Renewable Energy 227 (2024) 120540

Contents lists available at ScienceDirect

Renewable Energy

journal homepage: www.elsevier.com/locate/renene

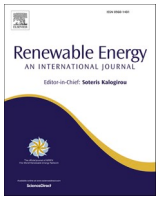

Design of small-scale hybrid energy systems taking into account generation and demand uncertainties

Juan M. Lujano-Rojas *, Rodolfo Dufo-López, Jesús Sergio Artal-Sevil, Eduardo García-Paricio

Department of Electrical Engineering, University of Zaragoza, Calle María de Luna 3, 50018, Zaragoza, Spain

A B S T R A C T

The adoption of energy systems powered by renewable sources requires substantial economic investments. Hence, selecting system components of an appropriate size becomes a critical step, which is significantly influenced by their distinct characteristics. Furthermore, the availability of renewable energy varies over time, and estimating this availability introduces considerable uncertainty. In this paper, we present a technique for the optimal design of hybrid energy systems that accounts for the uncertainty associated with resource estimation. Our method is based on stochastic programming theory and employs a surrogate model to estimate battery lifespan using a feedforward neural network (FFNN). The optimization analysis for system design was conducted using a genetic algorithm (GA) and the poplar optimization algorithm (POA). We assessed the effectiveness of the proposed technique through a hypothetical case study. The introduction of a surrogate model, based on an FFNN, resulted in an approximation error of 9.6 % for cost estimation and 20.6 % for battery lifespan estimation. The probabilistic design indicates an energy system cost that is 25.7 % higher than that obtained using a deterministic approach. Both the GA and POA achieved solutions that likely represent the global optimum.

1. Introduction

Adopting renewable energy at residential, commercial, and industrial levels is crucial for mitigating the adverse effects of human activities on the ecosystem. Engineers and designers have conducted thorough analyses on incorporating renewable energy at a smaller scale, particularly in rural electrification projects where connections to the distribution network are absent. Within this context, the general structure of the energy system includes wind and solar photovoltaic (PV) power sources. These are combined with a battery energy storage system (BESS) and a diesel generator to ensure a reliable supply of electricity.

Based on their experience, practitioners have identified several areas in which researchers could enhance current design methodologies. These areas encompass improving the performance and reliability of BESS [1], evaluating the temporal fluctuations and intrinsic variation of renewable resources, understanding energy demand and the uncertainties associated with estimating it, and selecting components based on their technical and economic characteristics through a complex optimization process [2], among others.

Investigators employ classical methods, metaheuristic methods, and a combination of both—referred to as hybrid methods—for the optimal design of hybrid energy systems. Classical methods encompass linear programming (LP), nonlinear programming, and dynamic programming (DP). In contrast, metaheuristic approaches include genetic algorithms (GAs), particle swarm optimization (PSO), simulated annealing, among others [1,2]. These techniques are widely utilized for both mono-objective optimization (MoOO) and multi-objective optimization (MuOO), adopting a deterministic perspective. MoOO focuses on minimizing costs, whereas MuOO aims to simultaneously minimize costs and emissions.

In the realm of probabilistic optimization, researchers frequently utilize methods such as stochastic programming (SP), robust optimization (RO), information gap decision theory (IGDT), and chance-constrained optimization (CCO), among other strategies. To date, SP has been extensively applied, demonstrating effective outcomes in various applications. IGDT, on the other hand, faces challenges in addressing multiple sources of uncertainty effectively. RO is commonly employed to model uncertainties related to energy market prices and renewable generation. Lastly, CCO is typically used to manage the uncertainties associated with load shedding [3].

Recently, Oyewole et al. [4] concentrated specifically on hydrogen production from renewable sources. These researchers devised an optimization model to consider the impacts of uncertainties associated with renewable resources and economic factors. This model utilized RO and was implemented through a mixed-integer quadratic constrained programming formulation, which was subsequently transformed into a

* Corresponding author.
E-mail addresses: lujano.juan@unizar.es (J.M. Lujano-Rojas), rdufo@unizar.es (R. Dufo-López), jsartal@unizar.es (J.S. Artal-Sevil), egarciap@unizar.es (E. García-Paricio).

https://doi.org/10.1016/j.renene.2024.120540
Received 16 October 2023; Received in revised form 11 March 2024; Accepted 19 April 2024
Available online 21 April 2024

mixed-integer linear programming (MILP) model.

Davoudkhani et al. [5] developed a design tool based on cloud model theory, which integrates fuzzy theory with probability statistics. This innovative approach characterizes the uncertainty of renewable resources and energy demand by employing both a normal membership function and a normal probability distribution. Regarding energy system design, the researchers advocated for the utilization of opposition-based learning alongside a gradient-based optimizer.

Jin and Li [6] utilized a hybrid fuzzy-SP method for the design of energy systems, incorporating the associated risk. This innovative model efficiently enables the consideration of design options that present a trade-off between cost and risk, indicating either low cost with high risk (suggesting lower reliability) or high cost with low risk.

Yuan et al. [7] formulated the design problem as a mixed-integer nonlinear programming (MINLP) problem and addressed it employing the firefly algorithm. This methodology resulted in a solution that exhibited greater reliability compared to those derived from deterministic implementations.

Gopila et al. [8] developed an optimization model that integrates the random decision forest (RDF) with the crystal structure algorithm (CryStAl), accounting for uncertainties in solar resources and energy demand.

Yadegari et al. [9] developed a MuOO model employing the augmented ε-constrained method. This methodology considers both economic and environmental factors within the optimization process. It facilitates the identification of impacts stemming from conventional and renewable energy generation, as well as combined heat and power (CHP) systems, on the operation of energy systems and the objectives mentioned previously.

Nowdeh et al. [10] tackled the uncertain parameters related to renewable resources and energy demand through the application of the unscented transformation method. They then formulated the optimization problem for energy system design as a nonlinear integer programming problem, which was resolved by employing a hybrid approach that combines the gray wolf optimization and honey bee mating optimization algorithms.

Li et al. [11] developed a management technique for energy systems incorporating cascade energy storage (encompassing hydro, wind, and solar systems) that synergizes deep learning with a double-layer nesting algorithm. To mitigate mathematical complexity, this technique amalgamates PSO and DP within the nesting algorithm framework. Concurrently, Lei et al. [12] tackled uncertainties through the application of scenario generation and reduction techniques. Subsequently, they articulated the optimization problem via a two-layer approach and resolved it employing an advanced lambda flow iteration strategy.

Dong et al. [13] addressed the uncertainties in renewable generation and electricity demand utilizing RO and interval analysis. Following this, they applied a constrained multi-objective transition algorithm to ascertain the optimal system size.

Furlan and You [14] investigated the hybridization of solar power generation through the integration of concentrated solar power (CSP) and PV technology to mitigate the high investment costs. Within this framework, they incorporated the uncertainty of diverse economic parameters into a MuOO model based on RO.

Technological advancements in nuclear power have encouraged researchers to investigate its integration with renewable energy sources. In this context, Bamshad and Safarzadeh [15] devised a model that probabilistically accounts for the uncertainties associated with economic and environmental factors. They integrated these uncertainties into an optimization model to ascertain the optimal system size. The authors employed a modified Metropolis Markov chain Monte Carlo method in conjunction with the Wilks' method, yielding a highly reliable solution. Following this, they utilized the WASP-IV software to determine the optimal system dimensions concerning cost and emissions.

Rizqi et al. [16] introduced a methodology that integrates adaptive PSO with machine learning to optimize the components of energy systems. This approach considers factors such as electric vehicles (EVs) and emission processes from a multi-objective perspective, accounting for uncertainty.

Divya et al. [17] proposed a design framework utilizing the black widow optimization (BWO) algorithm, which accounts for uncertainties arising from renewable resources and device reliability.

Wang and Ji [18] analyzed a supply chain and developed a mixed-integer optimization model designed to accommodate various sources of uncertainty. They transformed the equivalent probabilistic optimization problem into a deterministic format and then implemented a linearization process to enhance the mathematical tractability of the problem. Building upon this foundation, Dehshiri and Amiri [19] devised a supply chain optimization model utilizing a robust, scenario-based, possibilistic SP method. This model comprehensively addresses uncertainties that are both cognitive and stochastic in nature.

Er et al. [20] introduced a design tool for modern rural electrification that incorporates EVs, batteries, and fuel cells within the energy system framework. They formulated the design problem using a two-stage SP approach, employing scenario generation. Subsequently, this problem was addressed through the application of MILP.

Liu et al. [21] tackled the multi-objective economic dispatch (ED) problem through the application of the tunicate swarm algorithm (TSA), achieving a well-distributed set of solutions along the Pareto front. Extending this research, Bhavsar et al. [22] devised a hybrid method that merges data-driven and physics-based model-predictive techniques to address stochastic unit commitment (UC) and ED challenges. This innovative approach employs a data-driven machine learning framework to estimate mean generation costs, while solutions derived from the physics-based inverse problem delineate the UC and ED profiles.

Kim et al. [23] proposed a formulation that integrates a Markov decision process with reinforcement learning, incorporating specific strategies for storage dispatch through LP.

Belbachír et al. [24] proposed a MuOO technique that addresses critical aspects of distribution system operation, such as voltage profile and power losses. They implemented the long-term memory artificial hummingbird algorithm (AHA), observing promising outcomes.

Yang et al. [25] introduced an enhanced version of PSO algorithm for the optimal dimensioning of microgrids. This version accounts for general costs, levelized costs, and reliability factors.

Atawi et al. [26] developed a design strategy employing the multi-objective African vultures optimization algorithm (AVOA), which is applicable to both isolated and grid-connected architectures. Furthermore, the authors applied the Technique for Order of Preference by Similarity to Ideal Solution (TOPSIS) to identify the most suitable system configuration from the Pareto front.

Liu and Peng [27] introduced an optimization model founded on situation awareness theory and observed encouraging outcomes, particularly in balancing economic factors with the efficiency of renewable resource management.

Guan et al. [28] introduced a technique grounded in CCO. They utilized scenario generation and reduction methods to represent the uncertain parameter. Subsequently, they transformed the corresponding stochastic optimization problem into its deterministic counterpart and resolved it through multi-objective MILP. Finally, they applied the modified ε-constraint method to analyze the Pareto front.

Mottola et al. [29] developed a design methodology employing Taguchi arrays to represent uncertain variables, thereby significantly enhancing computational tractability throughout the optimization process.

Mohseni and Brent [30] developed a dimensioning model employing SP, wherein the design problem is addressed using the moth-flame optimization (MFO) algorithm.

Zhu et al. [31] introduced a dimensioning strategy founded on a two-stage methodology, which accounts for multiple sources of uncertainty and is supported by the Ebola optimization search algorithm

(EOSA).

Haghighat et al. [32] developed a two-stage RO approach, wherein the operational constraints are assessed using a second-order conic power flow model. In parallel, the optimization tasks are conducted using a parametric version of the column and constraint generation algorithm.

Billah et al. [33] introduced a management and sizing technique employing RO, which was implemented via a multi-agent system integrated with PSO.

The literature review presents a comprehensive array of power generation devices of interest, including modular nuclear power, CHP, and CSP. Furthermore, the dynamics of electricity demand have evolved, incorporating aspects such as the charging of EVs and their interaction with microgrid operations.

Conversely, numerous methodologies have been developed to appropriately dimension energy systems from economic and environmental standpoints, integrating various sources of uncertainty, predominantly associated with renewable generation. Among classical methodologies, LP, DP, MILP, and MINLP are widely recognized for addressing sizing and management issues such as ED and UC. Furthermore, it is pertinent to underscore that heuristic techniques, including PSO and its enhanced variants, are favored by designers of hybrid energy systems. These techniques are continually evolving in parallel with our deepening understanding of natural and cognitive processes.

The BESS is a critical component characterized by high capital costs, and its lifetime is contingent upon its utilization and associated aging mechanisms. Consequently, its frequent replacement can adversely affect the economic performance of the project, necessitating a meticulous assessment of the aging process across various battery technologies. Most previously referenced studies integrate precise models for estimating battery lifetime.

As information on the potential of renewable energy becomes increasingly accessible, integrating the estimation error of such databases into existing dimensioning models is crucial. However, this integration considerably escalates the computational complexity of the associated optimization problem. In the context of this paper, the inclusion of battery degradation processes requires multi-year simulations, thereby significantly augmenting the computational burden during optimization analysis. This issue represents an emerging challenge that has not been extensively discussed in most of the works mentioned previously.

This work proposes the integration of a surrogate model for estimating battery lifetime utilizing an artificial neural network (ANN) to reduce the computational effort associated with multi-year analyses—a concept not extensively explored in the existing technical literature on sizing hybrid energy systems. This model is subsequently embedded into an optimization framework based on SP, which is solved using an integer-coded heuristic technique. Pertinent to this, the methodology proposed herein accounts for the uncertainty of widely utilized public information sources, specifically referencing the Renewables.ninja [34] database.

In addition to GA and PSO, emerging heuristic techniques such as RDF and CryStAl [8], BWO [17], TSA [21], AHA [24], AVOA-TOPSIS [26], MFO [30], and EOSA [31], among others previously mentioned, have demonstrated effectiveness in solving complex problems. In this work, a recently developed heuristic method, the poplar optimization algorithm (POA) [35], is employed to design the energy system. To the best of our knowledge, this is the first instance of the POA being applied to the design of hybrid energy systems at a small scale.

This work is organized as follows: Section 2 delineates the model of the energy system under investigation. Section 3 provides a comprehensive explanation of the proposed methodology. Section 4 demonstrates the application of the suggested method through a case study. Finally, Section 5 summarizes the principal conclusions and remarks.

2. Model of a typical small-scale hybrid energy system

The energy system examined in this work consists of a wind and a PV generator, a BESS, a power converter, and a backup generator. The operating philosophy behind the system aims to satisfy load demand using energy from the wind and PV generators. Any surplus energy is stored in the BESS for later use. This approach minimizes the operating hours of the backup generator, thereby extending its lifespan and enhancing the overall economic performance of the system.

Fig. 1 shows the structure of the energy system. This section provides a brief overview of the models used to represent these components during simulation.

2.1. Wind generator

A wind turbine converts the kinetic energy of wind into electricity. Fig. 2 depicts the power curve of a typical low-capacity wind turbine, highlighting the cut-in, rated, and cut-out speeds. For each time step t, the wind speed at hub height, denoted as $W_{(t)}$, is referenced against the power curve, described by the function $f_W(W_{(t)}, z)$ provided by the manufacturer (where z represents parameters or specifics of the curve). The cut-in speed is the threshold at which power production begins. At the rated speed, the turbine generates its maximum power. Once it reaches the cut-out speed, the turbine reduces its output to ensure safety [36].

2.2. Photovoltaic generator

A PV panel facilitates the conversion of solar radiation into electricity. The simplified model outlined in equations (1) and (2) is used in this work. This model is particularly suitable for simulating systems equipped with maximum power point tracking. Power production, denoted by $P_{PV(t,v)}$, relies on the available solar irradiance $G_{(t)}$, ambient temperature $T_{A(t)}$, and several manufacturer-specific parameters (v) such as the nominal operating cell temperature $NOCT_{(v)}$, the temperature coefficient $\alpha_{PV(v)}$, and output power at standard test conditions $P_{STC(v)}$. Equation (1) determines the cell temperature $T_{C(t)}$, and equation (2) provides an approximation of the power generation [37]:

$$T_{C(t)} = T_{A(t)} + \left(\frac{NOCT_{(v)} - 20^{\circ}C}{800\ W/m^2}\right) G_{(t)}, \tag{1}$$

$$P_{PV(t,v)} = P_{STC(v)} \left\{ \frac{G_{(t)}}{1000} \left[1 + \alpha_{PV(v)} \left(T_{C(t)} - 25^{\circ}C\right)\right] \right\}. \tag{2}$$

2.3. Lead-acid battery bank

The BESS is pivotal as it endows the energy system with operational flexibility. Lead-acid battery (LAB) technology has been instrumental in the electrification of isolated regions. The predicted lifespan of an LAB hinges on its usage, as this determines the progression of corrosion and degradation over time. In light of this, the weighted Ah throughput approach is utilized [38–40].

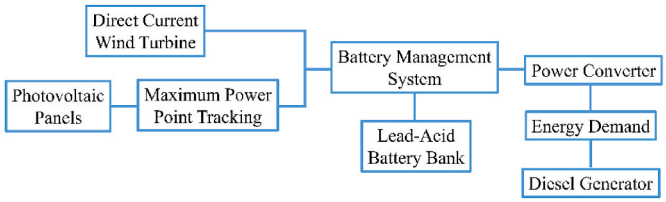

Fig. 1. Diagram of the hybrid energy system structure.

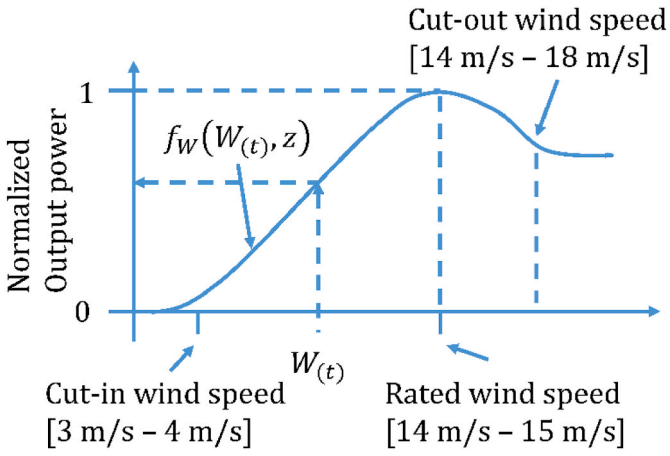

Fig. 2. Typical wind turbine power curve.

2.3.1. Assessing the hourly dynamic of a battery

Typically, the relationship between the cell voltage $U_{(t)}$, cell current $I_{(t)}$, and state of charge (SOC) at time t ($SOC_{(t)}$) is defined by the equation of Shepherd. This equation accounts for the effects of open circuit voltage, ohmic losses, and over-voltage. Equations (3) and (4) present the cell voltage for charging ($I_{(t)} > 0$) and discharging ($I_{(t)} < 0$), respectively [38–40]:

$$U_{(t)} = U_0 - gDOD_{(t)} + R^c_{(t)}\left(\frac{I_{(t)}}{C_{10(m)}}\right) + R^c_{(t)}M_c\left(\frac{I_{(t)}}{C_{10(m)}}\right)\left(\frac{SOC_{(t)}}{C_c - SOC_{(t)}}\right) \quad \forall\, I_{(t)} > 0, \tag{3}$$

$$U_{(t)} = U_0 - gDOD_{(t)} + R^d_{(t)}\left(\frac{I_{(t)}}{C_{10(m)}}\right) + R^d_{(t)}M_d\left(\frac{I_{(t)}}{C_{10(m)}}\right)\left(\frac{DOD_{(t)}}{C^d_{(t)} - DOD_{(t)}}\right) \quad \forall\, I_{(t)} \le 0, \tag{4}$$

where U_0 is the open-circuit voltage, g represents the variation of open-circuit voltage with SOC, $R^c_{(t)}$ and $R^d_{(t)}$ are the internal resistances for charging and discharging, respectively. M_c and M_d denote the resistances of charge-transfer processes during charging and discharging, respectively. C_c and $C^d_{(t)}$ are normalized capacities, $DOD_{(t)}$ is the depth of discharge, and $C_{10(m)}$ is the battery capacity for 10 h from manufacturer m. During charging periods, chemical processes related to the gassing phenomenon reduce the ability of the battery to store energy. This is taken into account in Equations (5) and (6) [38–40]:

$$SOC_{(t)} = SOC_{(t-\Delta t)} + \int_{t-\Delta t}^{t}\left\{\frac{I_{(\tau)} - I^G_{(\tau)}}{C_{10(m)}}\right\}d\tau, \tag{5}$$

$$I^G_{(t)} = \left(\frac{C_{10(m)}}{100}\right)\left(I^G_{0(t)}\right)exp\left(C_U\left[U_{(t)} - U^G_0\right] + C_T\left[T_{A(t)} - T^G_0\right]\right) \quad \forall\, I_{(t)} > 0, \tag{6}$$

where $I^G_{(\tau)}$ is the gassing current, C_U are the voltage parameters for gassing, U^G_0 is the gassing voltage, C_T is the temperature coefficient of gassing, and T^G_0 is the reference gassing temperature.

2.3.2. Incorporating the corrosion of the positive grid

The Shepherd model is also applied to study battery corrosion. It calculates the corrosion voltage for both charging and discharging conditions using equations (7) and (8) [38–40]:

$$U^c_{(t)} = U^c_0 - \left(\frac{10}{13}\right)gDOD_{(t)} + R^c_{(t)}\left(\frac{I_{(t)}}{2C_{10(m)}}\right) + R^c_{(t)}M_c\left(\frac{I_{(t)}}{2C_{10(m)}}\right)\left(\frac{SOC_{(t)}}{C_c - SOC_{(t)}}\right) \quad \forall\, I_{(t)} > 0, \tag{7}$$

$$U^c_{(t)} = U^c_0 - \left(\frac{10}{13}\right)gDOD_{(t)} + R^d_{(t)}\left(\frac{I_{(t)}}{2C_{10(m)}}\right) + R^d_{(t)}M_d\left(\frac{I_{(t)}}{2C_{10(m)}}\right)\left(\frac{DOD_{(t)}}{C^d_{(t)} - DOD_{(t)}}\right) \quad \forall\, I_{(t)} \le 0, \tag{8}$$

where $U^c_{(t)}$ is the corrosion voltage, and U^c_0 is the corrosion voltage under open-circuit conditions when the battery is fully charged. The characteristics of the corrosion layer and its resistance are examined using equation (9) through (12) [38–40]:

$$\Delta W_{(t)} = \begin{cases} k_{sp}\left(y^{0.6}\right) \;\middle|\; y = \left[\Delta W_{(t-\Delta t)}/\left(k_{sp}\right)\right]^{\frac{1}{0.6}} + \Delta t;\ U^c_{(t)} < 1.74 \\ \Delta W_{(t-\Delta t)} + \left(k_{sp}\right)\Delta t;\ U^c_{(t)} \ge 1.74 \end{cases}, \tag{9}$$

$$\Delta R_{(t)} = \Delta R_{max}\left(\frac{\Delta W_{(t)}}{\Delta W_{max}}\right), \tag{10}$$

$$\Delta C^c_{(t)} = \Delta C^c_{max}\left(\frac{\Delta W_{(t)}}{\Delta W_{max}}\right), \tag{11}$$

$$\Delta W_{max} = 365 \times 24 \times \left(FL_{(m)}\right)\left(k^{sp}_{max}\right), \tag{12}$$

where $\Delta W_{(t)}$ represents the variation in the thickness of the corrosion layer, k_{sp} is the corrosion speed coefficient, $\Delta R_{(t)}$ is the increase in the internal resistance of the corrosion layer, ΔR_{max} is the maximum resistance of the corrosion layer, ΔW_{max} is the maximum corrosion layer thickness, $\Delta C^c_{(t)}$ is the capacity loss related to corrosion, ΔC^c_{max} is the maximum capacity loss related to corrosion, and k^{sp}_{max} is the corrosion speed parameter at the corresponding float voltage. The latter is determined by evaluating the Lander curve. Finally, $FL_{(m)}$ is the battery float lifetime for manufacturer m.

2.3.3. Incorporating the active mass degradation

The weighted Ah throughput method accounts for active mass degradation using several parameters related to the SOC, the elapsed time under a low SOC, the discharging current, and the number of incomplete charging cycles. These concepts are mathematically represented in equations (13)–(16). Fig. 3 depicts concepts of interest during full and partial charging operations. Full and partial conditions are determined by the parameter SOC^{MAX}_{LIM}, which is typically set at 0.9. The influence of a low SOC is represented by the factor $min\{SOC_{(\tau)}|\tau \in [t_B, t]\}$ and the effect of the time elapsed at such a SOC is captured by the time

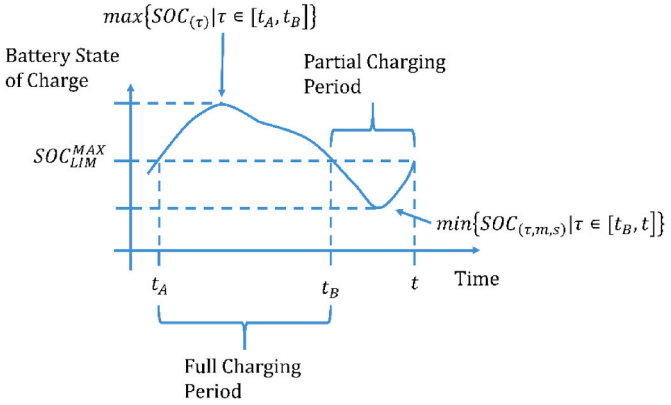

Fig. 3. Definition of battery operation under full and partial conditions.

interval $t - t_B$. Equations (13) and (14) determine the SOC factor $f_{(t)}^{soc}$ incorporating these definitions [38–40]:

$$f_{(t)}^{soc} = 1 + \left[c_0^{soc} + c_{min}^{soc}\left(1 - min\{SOC_{(\tau)}|\tau \in [t_B, t]\}\right) f_{(t)}^{I} \Delta t_{(t)}^{soc}\right], \tag{13}$$

$$\Delta t_{(t)}^{soc} = t - t_B, \tag{14}$$

in equations (13) and (14), c_0^{soc} and c_{min}^{soc} are coefficients of the SOC impact factor associated with the slope and minimum SOC. The term $f_{(t)}^{I}$ represents the current factor, and $\Delta t_{(t)}^{soc}$ is the elapsed time since the last full battery charge. The influence of the discharging current on battery aging is captured by the current factor $f_{(t)}^{I}$, as shown in equation (15) [38–40]:

$$f_{(t)}^{I} = \left(\sqrt{\frac{I_r}{I_{(t)}^{1th}}}\right)\left(\sqrt[3]{exp\left(\frac{q}{3.6}\right)}\right). \tag{15}$$

In the equation above, I_r is a reference current, and $I_{(t)}^{1th}$ is the discharging current observed at the start of the partial cycle period, while q represents the number of cycles with insufficient charging. This formulation emphasizes the discharging current at the outset of the partial cycle. Furthermore, the impact of suboptimal charging cycles is integrated by weighting the number of cycles with the factor Δq from equation (16). This factor is contingent on the maximum SOC attained [38–40]:

$$\Delta q = \frac{0.0025 - \left(0.95 - max\{SOC_{(\tau)}|\tau \in [t_A, t_B]\}\right)^2}{0.0025}. \tag{16}$$

The degree of acid stratification is incorporated into the aging model using the factor $f_{(t)}^{ST}$ of equation (17), which takes into account the effects of gassing and diffusion phenomena, as described in equation (18) through (21). The increase in acid stratification due to partial cycling operation is accounted for by the minimum SOC $min\{SOC_{(\tau)}|\tau \in [t_B, t]\}$. On the other hand, the reduction in stratification due to gassing and diffusion is reflected by considering the gassing current $I_{0(t)}^{G}$ and the ambient temperature $T_{A(t)}$. The influence of these phenomena on acid stratification is assessed by integrating the difference between the factors for acid stratification increase $\Delta f_{(t)}^{+}$ and reduction $\Delta f_{(t)}^{-}$ [38–40]:

$$f_{(t)}^{ST} = f_{(t-\Delta t)}^{ST} + \int_{t-\Delta t}^{t}\left(\Delta f_{(\tau)}^{+} - \Delta f_{(\tau)}^{-}\right)d\tau, \tag{17}$$

$$\Delta f_{(t)}^{+} = C_P\left(1 - min\{SOC_{(\tau)}|\tau \in [t_B, t]\}\right) exp\left(-3 f_{(t)}^{ST}\right)\left(\frac{\left|I_{(t)}^{d}\right|}{I_r}\right), \tag{18}$$

$$\Delta f_{G(t)}^{-} = C_M\sqrt{\frac{100}{C_{10(m)}}}\left(\frac{I_{0(t)}^{G}}{I_0^{G}}\right)\exp\left(C_U\left[U_{(t)} - U_r\right] + C_T\left[T_{A(t)} - T_0^{G}\right]\right), \tag{19}$$

$$\Delta f_{D(t)}^{-} = \frac{8 D_Z}{(Z_D)^2} f_{(t-\Delta t)}^{ST} 2^{\left(T_{A(t)} - 293.15\right)/10}, \tag{20}$$

$$\Delta f_{(t)}^{-} = \Delta f_{D(t)}^{-} + \Delta f_{G(t)}^{-}. \tag{21}$$

In equation (17) through (21), $I_{(t)}^{d}$ is the discharging current. C_P represents the coefficient for the increase in acid stratification, while C_M denotes the coefficient for its reduction. I_0^{G} is the normalized gassing current, correlated with U_0^{G} and T_0^{G}, U_r is the reference voltage associated with the reduction of acid stratification. D_Z is the diffusion constant, and Z_D is the typical height of a battery cell. $\Delta f_{G(t)}^{-}$ is the factor concerning the reduction of acid stratification due to gassing, and $\Delta f_{D(t)}^{-}$ pertains to the reduction due to diffusion. Lastly, the cumulative effects of acid stratification are encapsulated by the factor $f_{(t)}^{A}$ as described in equation (22) [38–40]:

$$f_{(t)}^{A} = 1 + f_{(t)}^{ST}\sqrt{\frac{I_r}{I_{(t)}^{1th}}}. \tag{22}$$

The factors computed up to this point are integrated into the weighted Ah estimation, denoted as $Z_{(t)}^{W}$, as defined in equation (23). Subsequently, the capacity loss due to degradation, represented as $\Delta C_{(t)}^{d}$, is estimated using equation (24) [38–40].

$$Z_{(t)}^{W} = \frac{1}{C_{10(m)}}\int_0^t \left|I_{(t)}^{d}\right| f_{(t)}^{soc} f_{(t)}^{A} dt \tag{23}$$

$$\Delta C_{(t)}^{d} = \Delta C_{max}^{d}\exp\left(-C_Z\left\{1 - \frac{Z_{(t)}^{W}}{1.6\left[Z_{I(m)}\right]}\right\}\right) \tag{24}$$

where ΔC_{max}^{d} is the maximum capacity loss associated with degradation, C_Z is a parameter related to the capacity loss due to degradation, and $Z_{I(m)}$ represents the number of cycles under standard conditions. After estimating the progression of the aging mechanism, the internal resistance for both charging and discharging, the gassing current, and the battery capacity are updated for the specific time instant t [38–40]:

$$R_{(t)}^{c} = R_{(0)}^{c} + \Delta R_{(t)} \tag{25}$$

$$R_{(t)}^{d} = R_{(0)}^{d} + \Delta R_{(t)} \tag{26}$$

$$I_{0(t)}^{G} = I_0^{G} + \Delta I_0^{G}\left(\frac{\Delta R_{(t)}}{\Delta R_{max}}\right) \tag{27}$$

$$C_{(t)}^{d} = C_{(0)}^{d} - \Delta C_{(t)}^{c} - \Delta C_{(t)}^{d} \tag{28}$$

The process of battery performance analysis, corrosion of the positive grid study, estimation of active mass degradation, and parameter updates is sequentially repeated until the normalized battery capacity $C_{(t)}^{d}$ drops to a value lower than 0.8. At that point, the battery is considered to have reached the end of its operational lifetime [38–40].

2.4. Power converter

The power converter provides a link between the renewable power sources and the BESS operating in direct current (DC), and the load demand and backup generator operating in alternating current (AC). While simulation models used for energy system sizing often focus on efficiency variations, in this work, the converter efficiency $\eta_{CNV(t)}$ at time t is determined as per (29):

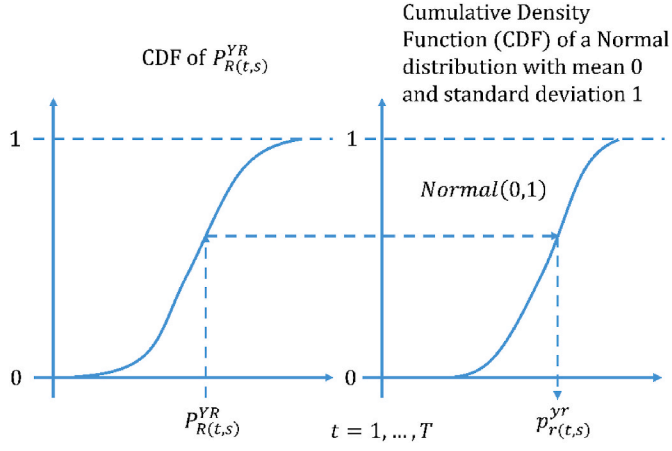

Fig. 4. Probability transformation to normalize the yearly profile for scenario creation.

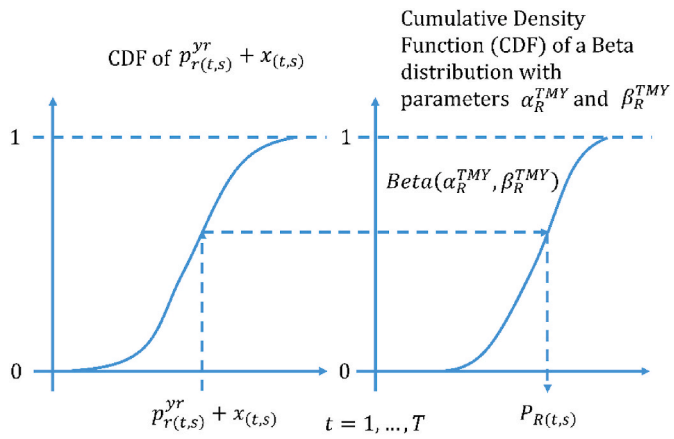

Fig. 5. Probability transformation to normalize the yearly random time series.

$$\eta_{CNV(t)} = \frac{P_{L(t)}}{\alpha_C^A \times P_C^{MAX} + \alpha_C^B \times P_{L(t)}}, \tag{29}$$

where $P_{L(t)}$ is the AC load demand, P_C^{MAX} is the rated power of the converter, and α_C^A and α_C^B are parameters to be calibrated using experimental data. It is imperative to note that this represents a simplified expression of a definition commonly employed, wherein the denominator is typically formulated as a second-order polynomial. In this work, a straightforward linear expression has been selected to obviate the need for solving the second-order polynomial at each hour. Detailed information is available in Ref. [41].

2.5. Backup generator

The backup generator ensures a high-reliability system, given that its power production can be controlled. The simulation models commonly used for energy system dimensioning are designed to accurately estimate fuel consumption. Typically, a linear function is used, as illustrated in (30) [42]:

$$F_{G(t,y)} = \alpha_{G(y)}^A \times P_{G(y)}^{MAX} + \alpha_{G(y)}^B \times P_{G(t)}, \tag{30}$$

where $F_{G(t,y)}$ is the fuel consumption at time t for manufacturer y, $P_{G(y)}^{MAX}$ is the rated power of the backup generator for manufacturer y, $P_{G(t)}$ is the power production of the backup generator for manufacturer y, and $\alpha_{G(y)}^A$ and $\alpha_{G(y)}^B$ are parameters obtained from experimental data.

2.6. Load demand

The AC load demand can be estimated by summing the individual requirements of each household appliance. Thus, $P_{D(l)}$ is the power of a specific device l ($l = 1, \ldots, L$), which operates for $\Delta h_{(l)}$ hours and is typically connected to the system between the hours $h_{(l)}^{min}$ and $h_{(l)}^{max}$. This information is valuable for modeling long-term electricity demand.

Table 1
Description of a typical GA individual.

Element of individual $k_{(n)}$	Description
$v \in [1, V]$	Index for solar panel manufacturers
$d \in [1, D]$	Number of panels in parallel
$z \in [1, Z]$	Index for wind turbine manufacturers
$j \in [1, J]$	Number of wind turbines
$m \in [1, M]$	Index for battery manufacturers
$o \in [1, O]$	Number of batteries in parallel
$y \in [1, Y]$	Index for generator manufacturers

3. Proposed methodology

The methodology introduced in this work aims to determine the rated power of the wind and PV generators, BESS, power converter, and backup generator. It takes into account the uncertainty introduced by renewable resource estimation and aims to minimize the expected net present cost (NPC) while adhering to a specific, intrinsically probabilistic reliability condition. The optimization problem and its corresponding solution method are presented in the subsequent sections.

3.1. Formulation of the optimization problem

The techno-economic analysis is designed to minimize the NPC over the operational lifetime of the system. The NPC is influenced not only by capital and replacement costs but also by the availability of natural resources and renewable energy. This is because these factors directly affect fuel consumption and the operational hours of the backup generator. As a result, the NPC is significantly affected by the uncertainty associated with estimating wind and solar resources. The objective function in focus is presented in equation (31), which seeks to minimize the expected value $\mathbb{E}\{\cdot\}$ of the total NPC:

$$min\ \mathbb{E}\{NPC_{(k)}\} \tag{31}$$

In equation (31), the variable $NPC_{(k)}$ denotes the NPC for a specific energy system configuration defined by the vector $\boldsymbol{k}$. The energy system is designed to ensure a specific reliability level based on DM needs. Accordingly, the optimization problem is subject to constraint (32):

$$\mathbb{P}\{EIU_{(k)} \le \varepsilon\} \ge 1 - \delta \tag{32}$$

$$EIU_{(k)} = \frac{\sum ENS}{\sum P_L} \tag{33}$$

In equation (32), $EIU_{(k)}$ represents the energy index of unreliability (EIU) for the configuration specified by the vector $\boldsymbol{k}$. This index normalizes the annual energy not supplied (ENS) relative to the total electricity demand over the year. The parameter ε allows DM to set the desired reliability level, while δ defines the extent to which this probabilistic condition is met. That is, the probability $\mathbb{P}\{\cdot\}$ that $EIU_{(k)} \le \varepsilon$ is less than or equal to ε must be at least $1 - \delta$. Typically, δ is assigned a small value.

In this study, uncertainty associated with renewable generation is addressed through a set of representative scenarios ($s = 1, \ldots, S$). For every scenario, the energy system must be operated safely, adhering to constraints (34)–(41). Equations (34)–(36) dictate that for a specific battery manufacturer, m, the state of charge ($SOC_{(t)}$), current ($I_{(t)}$), and voltage ($U_{(t)}$) must remain within the prescribed range. These ranges are provided by the recommendations of the manufacturer and are applicable for each time step t ($t = 1, \ldots, T$) and for every scenario s:

$$SOC_{BT(m)}^{MIN} \le SOC_{(t)} \le SOC_{BT(m)}^{MAX} \tag{34}$$

$$I_{BT(m)}^{MAX} \le I_{(t)} \le I_{BT(m)}^{MAX} \tag{35}$$

$$U_{BT(m)}^{MIN} \le U_{(t)} \le U_{BT(m)}^{MAX} \tag{36}$$

Equation (37) ensures that the power converter is not operated beyond its rated capacity (P_C^{MAX}). In this study, we have linked the rated capacity of the power converter to the maximum load demand. This simplification enables us to consider only a single manufacturer throughout the optimization process:

$$0 \le P_{C(t)} \le P_C^{MAX} \tag{37}$$

In (37), $P_{C(t)}$ represents the power converted at time t for scenario s. Equation (38) sets an operational condition for the backup generator (y) when it is in use. Consequently, the power production $P_{G(t)}$ must remain

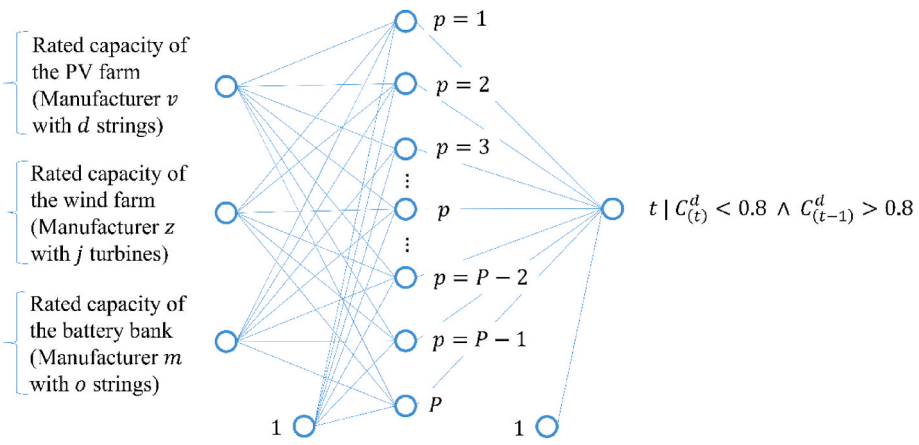

Fig. 6. Feedforward neural network for battery lifetime estimation.

between $P_{G(y)}^{MIN}$ and $P_{G(y)}^{MAX}$ for every time step $t = 1, \ldots, T$ and across all scenarios $s = 1, \ldots, S$.

$$P_{G(y)}^{MIN} \leq P_{G(t)} \leq P_{G(y)}^{MAX} \tag{38}$$

Equations (39)–(41) represent the power balance, which must be satisfied regardless of the manufacturers involved, the specific time step, or the scenario considered.

$$j \times P_{W(t)} + d \times P_{PV(t)} \pm o \times P_{BT(t)} + ENS_{(t)} - \left(P_{L(t)} + ES_{(t)}\right) = P_{G(t)} \tag{39}$$

$$0 \leq ENS_{(t)} \leq \infty \tag{40}$$

$$0 \leq ES_{(t)} \leq \infty \tag{41}$$

In equation (39), j represents the number of wind turbines in the wind generator, d signifies the number of PV panels connected in parallel, and o denotes the number of batteries connected in parallel. The variables $ENS_{(t)}$ and $ES_{(t)}$ correspond to the energy not supplied (ENS) and energy surplus at time t for scenario s, respectively. They are modeled as a generator and a dump load to ensure a feasible solution during the simulation process. $P_{BT(t)}$ is the power of the battery, calculated using the cell current ($I_{(t)}$) and voltage ($U_{(t)}$), and the battery bank configuration (which considers the number of batteries connected in series and parallel).

3.2. Scenario-generation of renewable power and load demand

Estimating natural resources is a critical and complex task essential for the development and deployment of clean energies. Scientists assess these resources by measuring long-term meteorological variables or by analyzing satellite images. From these efforts, researchers have compiled databases on a global scale, which contain relevant statistical information on wind speed, ambient temperature, and solar irradiance for general purposes.

A notable example is the model devised by Pfenninger and Staffell [43,44]. Among various models, the researchers utilized the Modern-Era Retrospective Analysis for Research and Applications, Version 2 (MERRA-2) technique to estimate meteorological variables on a global scale. They analyzed PV power production time series from over a thousand European locations spanning thirty years. Through this extensive data, the authors studied variability and correlation, introducing a mechanism to reduce bias error [43]. A similar approach was adopted for analyzing wind generation across twenty-three European locations, resulting in a notable reduction of bias error [44]. The computational foundation of these studies is available in the Renewables.ninja [34] database.

Recently, Ortiz et al. [45] refined the estimates provided by Renewables.ninja for Norwegian locations and achieved promising results. In this study, we extracted critical information about the estimation error of Renewables.ninja and incorporated it into our optimization model designed for sizing and optimizing hybrid energy systems. We used the discrepancy between the estimates of Renewables.ninja and the actual data, along with the root mean square error (RMSE) presented in Ref. [45] for PV and wind power, to construct PV and wind generation scenarios for the typical meteorological year (TMY).

The methodology employed in this study to develop scenarios representing the uncertainty of resource estimation is based on the procedure outlined in Refs. [46,47] for synthesizing wind speed time series.

Scenario generation for PV and wind power begins by downloading the time series of wind speed $W_{(t)}$, solar irradiance $G_{(t)}$, and ambient temperature $T_{A(t)}$ from the Renewables.ninja [34] website, which bases its data on the MERRA-2 methodology. Given that the methodology applied is consistent for both wind and PV generation, we use the time series $R_{(t)}^{TMY}$ to represent them. For wind generation, $R_{(t)}^{TMY}$ equates to $W_{(t)}$, and for PV generation, $R_{(t)}^{TMY}$ is $G_{(t)}$. Similarly, the rated capacity of a wind turbine and a single string of PV panels (P_{STC}) are both represented by the variable P_N. It is important to note that this study does not account for the uncertainty in ambient temperature estimation. The power curve representing the wind turbine is f_W, and PV generation is determined using equations (1) and (2). For notational simplicity, both f_W and the models in equations (1) and (2) are represented using the function f_R.

After obtaining wind speed, solar irradiance, and temperature data from the Renewables.ninja [34] database, we evaluate equation (42) for a specified rated power of either the wind turbine or the PV generator (P_N). This procedure converts the wind speed or solar irradiance TMY from their respective units into power, which serves as the primary profile for scenario generation. This outcome is represented by the time series $P_{R(t)}^{TMY}$.

$$P_{R(t)}^{TMY} = f_R\left(R_{(t)}^{TMY}, P_N, T_{A(t)}\right) \tag{42}$$

Having calculated the main profile, it becomes necessary to determine the mean and standard deviation of the estimation error. For this purpose, we use equations (43) and (44) to estimate the mean ($\mu_{(t)}$) and standard deviation ($\sigma_{(t)}$), respectively:

$$\mu_{(t)} = max\left(0, P_{R(t)}^{TMY} - \mu_R^{TMY} \times P_N\right) \tag{43}$$

$$\sigma_{(t)} = \sigma_R^{TMY} \times P_N \tag{44}$$

In this context, μ_R^{TMY} and σ_R^{TMY} represent the mean and standard deviation of the estimation error, respectively. For wind power scenario

creation, the values are $\mu_R^{TMY} = 0.0169$ and $\sigma_R^{TMY} = 0.215$. Conversely, for PV power scenario generation, they are $\mu_R^{TMY} = 0.0071$ and $\sigma_R^{TMY} = 0.1398$ [45].

Considering each day individually and using the index h (where $h = 1, \ldots, H = 24$ represents the hour of the given day), we estimate the daily profile according to equation (45):

$$P_{R(h,s)}^{DL} = \begin{cases} 0;\ CDF^{-1}\left(RAND, \mu_{(h)}, \sigma_{(h)}\right) < 0 \\ P_N; CDF^{-1}\left(RAND, \mu_{(h)}, \sigma_{(h)}\right) > P_N \\ CDF^{-1}\left(RAND, \mu_{(h)}, \sigma_{(h)}\right); else \end{cases} \quad (45)$$

where *RAND* is a uniform random number on the interval [0,1], $\mu_{(h)}$ and $\sigma_{(h)}$ represent the mean and standard deviation at time h, respectively. The term CDF^{-1} is the inverse cumulative distribution function (CDF) of a normal distribution with mean $\mu_{(h)}$ and standard deviation $\sigma_{(h)}$.

Finally, the profile for PV or wind power for the corresponding day is represented by $P_{R(h,s)}^{DL}$. It is important to highlight that the relationship between the indices $t = 1, \ldots, T$ and $h = 1, \ldots, H$ can be easily established using a reshaping process. This procedure allows us to simulate days when PV or wind generation $P_{R(h,s)}^{DL}$ is higher or lower than that specified by the TMY $P_{R(t)}^{TMY}$, depending on the value of *RAND*.

By repeating this procedure for the remainder of the days in a year, we obtain an annual profile of PV and wind power $P_{R(t,s)}^{YR}$ that exhibits the desired estimation error. Next, we need to convert the profile $P_{R(t,s)}^{YR}$ into a time series that follows the behavior of a normal distribution with a mean of zero and a standard deviation of 1. To achieve this, we employ the probability transformation illustrated in Fig. 4, resulting in the time series $p_{y(t,s)}^{yr}$ [28].

Having obtained a normalized profile, our next step is to produce a random time series $x_{(t,s)}$ that maintains a correlation degree similar to the original PV or wind power series. To achieve this, we refer to equation (46):

$$x_{(t,s)} = x_{(t-1,s)} + RANG\left(0, \sqrt{1-\rho^2}\right) \quad (46)$$

In this equation, *RANG* is a random number derived from a normal distribution with a mean of zero and a standard deviation of $\sqrt{1-\rho^2}$. Here, ρ represents the one-lag autocorrelation coefficient. By adding the normalized profile $p_{y(t,s)}^{yr}$ to the random series $x_{(t,s)}$, we obtain a series that aligns with the profile $p_{y(t,s)}^{yr}$ and maintains the autocorrelation ρ.

The final step involves transforming the series $p_{y(t,s)}^{yr} + x_{(t,s)}$ to adhere to the probability function of the original PV or wind power series. We operate under the assumption that both PV and wind power follow a beta distribution, characterized by parameters α_R^{TMY} and β_R^{TMY}. The necessary probability transformation is illustrated in Fig. 5, yielding the series $P_{R(t,s)}$.

Because the beta distribution operates with numbers within the [0,1] interval, we must multiply the series $P_{R(t,s)}$ by the rated capacity P_N.

In reference to Sub-section 2.6, for a specific day, we mandate the power block $P_{D(l)}$ and its duration $\Delta h_{(l)}$ to commence at a time chosen randomly between $h_{(l)}^{min}$ and $h_{(l)}^{max}$ using an integer random number generator. We iterate this process for each device ($l = 1, \ldots, L$) and every day of the year. Subsequently, we sum the power demands of all devices to form the complete yearly load scenario.

3.3. Implementation of the stochastic programming model

Solving the optimization problem involves determining the combination of manufacturers that minimizes equation (31) while satisfying constraints (32)–(41). Formulating this optimization problem in a linear manner is challenging due to the complexities of the LAB aging model. As a result, techniques such as MILP and MINLP are seldom employed to handle the specificities of the problem addressed in this study. Among various evolutionary techniques, the GA stands out as a widely used optimization method for this problem and is available in several commercial programs for energy system analysis. Moreover, the POA is a relatively new routine with advanced searching capabilities. The implementation of each of these techniques is briefly described in the next sub-sections.

3.3.1. Integer-coded genetic algorithm

The implementation of the GA for optimal sizing of energy systems uses integer coding [48]. This approach utilizes a list of manufacturers for PV panels, wind turbines, batteries, and backup generators. Based on this data, the structure of a typical individual (represented by $n = 1, \ldots, N$) is defined by the vector $\boldsymbol{k}_{(n)}$ in equation (47). A comprehensive description of each of its elements is provided in Table 1:

$$\boldsymbol{k}_{(n)} = [\, v \quad d \quad z \quad j \quad m \quad o \quad y \,] \quad (47)$$

In equation (47), the variables V, Z, M, and Y represent the number of manufacturers for PV panels, wind turbines, batteries, and backup generators, respectively. Similarly, the variables D, J, and O denote the maximum number of PV panels, wind turbines, and batteries that can be connected in parallel, respectively.

After identifying the characteristics of a typical individual, we construct the population using an integer matrix $\boldsymbol{K}$ as indicated in equation (48).

$$\boldsymbol{K} = \begin{bmatrix} \boldsymbol{k}_{(1)} \\ \vdots \\ \boldsymbol{k}_{(n)} \\ \vdots \\ \boldsymbol{k}_{(N)} \end{bmatrix} \quad (48)$$

where the index N denotes the population size. During the optimization process, the GA must evaluate each individual to compute the NPC ($NPC_{(k)}$) for the given configuration ($\boldsymbol{k}_{(n)}$) and scenario ($s = 1, \ldots, S$), subsequently calculating the expected value $\mathbb{E}\{NPC_{(k)}\}$. The NPC is significantly influenced by battery lifetime, as the battery is a costly device, and its replacement demands considerable financial resources. We have incorporated the aging model described in Section 2.3 to determine the lifespan of the battery under specific system configurations. It is vital to emphasize that utilizing this model necessitates a multi-year, hourly simulation for each scenario, making the process computationally demanding.

The estimation of battery lifetime can be decoupled from the optimization process using an ANN, thereby reducing the computational burden during the GA implementation. Alternatively, EIU can be estimated by simulating a single year (8760 h) without accounting for the impact of the aging mechanism on battery parameters.

Fig. 6 illustrates the structure of the feedforward neural network (FFNN) used, which consists of P hidden units. This ANN takes the elements of the vector $\boldsymbol{k}_{(n)}$ as its input and estimates the lifetime of the battery. In other words, it predicts the moment (t) when the normalized capacity ($C_{(t)}^d$) drops from a value greater than 0.8 to one less than 0.8, indicating that the battery is no longer useable.

Regarding the reliability analysis, it is conducted without considering the influence of the battery aging process on its parameters ($R_{(t)}^c$ and $R_{(t)}^d$). This implies that the battery cell voltage is computed based on equations (49) and (50) for charging and discharging, respectively, using the initial values of $R_{(0)}^c$ and $R_{(0)}^d$ over a single year (8760 h):

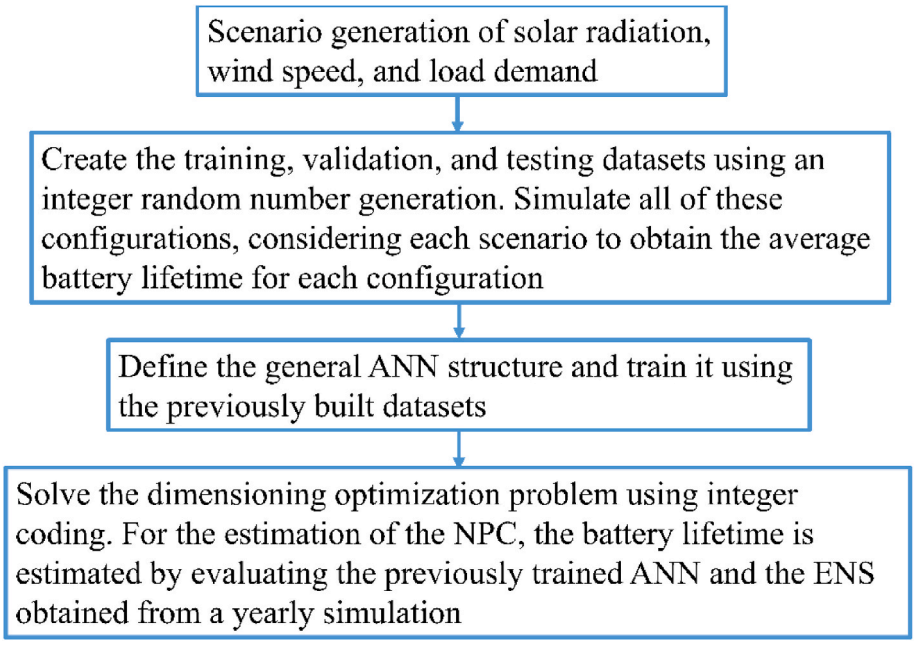

Fig. 7. Flowchart of the proposed methodology.

Table 2
Characteristics of electricity load demand.

l	$\Delta h_{(l)}$ (h)	$P_{D(l)}$ (W)	$h_{(l)}^{min}$ (h)	$h_{(l)}^{max}$ (h)
1	24	120	1	24
2	5	72	1	24
3	3	50	1	24
4	4	15	1	24

Table 3
List of PV panel manufacturers.

v	$P_{STC(v)}$ (W)	$\alpha_{PV(v)}$ (%/°C)	$NOTC_{(v)}$ (°C)	Capital cost (€)
2	200	−0.35	47	146.74
3	245	−0.44	47.5	156.60
4	250	−0.44	47.5	157.44
5	325	−0.41	45	164.96
6	330	−0.41	45	165.15
7	405	−0.35	45	164.06
8	410	−0.341	42.5	163.74
9	410	−0.35	45	163.74
10	415	−0.341	42.5	163.39
11	450	−0.347	42.5	160.20
12	500	−0.35	45	153.46
13	530	−0.35	45	148.29
14	535	−0.35	46	147.35
15	540	−0.341	42.5	146.38
16	540	−0.35	45	146.38
17	545	−0.349	45	145.40
18	545	−0.35	48	145.40
19	550	−0.349	45	144.39
20	550	−0.35	46	144.39
21	555	−0.35	45	143.37

$$U_{(t)} = U_0 - gDOD_{(t)} + R^c_{(0)}\left(\frac{I_{(t)}}{C_{10(m)}}\right) + R^c_{(0)}M_c\left(\frac{I_{(t)}}{C_{10(m)}}\right)\left(\frac{SOC_{(t)}}{C_c - SOC_{(t)}}\right) \quad \forall\, I_{(t)} > 0 \tag{49}$$

Table 4
List of wind turbine manufacturers.

z	Rated power (W)	Capital cost (€)
2	400	5002.02
3	900	5513.44
4	1000	5615.72
5	1800	6433.98
6	2500	7149.96
7	3000	7661.37
8	5000	9707.03
9	7500	12264.09

Table 5
List of backup generator manufacturers.

y	$P_{G(y)}^{MAX}$ (W)	$P_{G(y)}^{MIN}$ (W)	Capital cost (€)
2	3000	1500	6356.73
3	3500	1750	7428.48
4	3800	1900	8071.53
5	6500	3250	13858.98
6	7000	3500	14930.73
7	7200	3600	15359.43

$$U_{(t)} = U_0 - gDOD_{(t)} + R^d_{(0)}\left(\frac{I_{(t)}}{C_{10(m)}}\right) + R^d_{(0)}M_d\left(\frac{I_{(t)}}{C_{10(m)}}\right)\left(\frac{DOD_{(t)}}{C^d_{(0)} - DOD_{(t)}}\right) \quad \forall\, I_{(t)} \le 0 \tag{50}$$

The proposed technique for optimal sizing of hybrid energy systems under uncertainty can be summarized as follows.

Step 1: By analyzing the database of manufacturers, establish the variables V, D, Z, J, M, O, and Y as defined in Table 1. All of these variables are assumed to represent large numbers.
Step 2: Establish the voltage for the DC bus, which determines the number of PV panels and batteries connected in series. Also, set the economic parameters, including capital, operation and maintenance costs, inflation and interest rates, and the lifespan of the project.

Table 6
List of battery manufacturers.

m	$C_{10(m)}$ (Ah)	$Z_{I(m)}$ (cycles)	$SOC_{BT(m)}^{MIN}$	$FL_{(m)}$ (yr)	Capital cost (€)
2	200	1415	0.3	10	117.04
3	300	1415	0.3	10	129.66
4	600	1415	0.3	10	167.52
5	800	1415	0.3	10	192.76
6	1000	1415	0.3	10	218.00
7	1500	1415	0.3	10	281.10
8	2000	1415	0.3	10	344.20
9	2500	1415	0.3	10	407.30
10	3000	1415	0.3	10	470.40
11	460	1479	0.4	12	149.85
12	1156	1479	0.4	12	237.69
13	1900	1479	0.4	12	331.58
14	225	513	0.3	10	120.19
15	360	513	0.3	10	137.23
16	250	511	0.4	10	123.35
17	275	511	0.4	10	126.50
18	305	511	0.4	10	130.29
19	10	363	0.4	10	93.06
20	24	363	0.4	10	94.83
21	55	363	0.4	10	98.74
22	200	363	0.4	10	117.04

Table 7
Economic parameters.

Inflation rate (%)	Nominal rate (%)	Proyect lifetime (yr)	Gasoline price (€/liter)
2	3	40	1.641

Table 8
Settings for FFNN training.

Learning rate (%)	Iteration number	Hidden layers (P)	Training portion (%)	Validation portion (%)	Testing portion (%)
0.1	100	15	80	10	10

Table 9
Settings of genetic algorithm and problem constraints.

Population size (N)	Iterations (B)	Crossover rate (%)	Mutation rate (%)
25	100	80	10

Table 10
Settings of poplar optimization algorithm and problem constraints.

Population size (N)	Iterations (B)	δ_{POA}	α_{POA}	β_{POA}
25	100	0.6	0.6	1.4

Step 3: Set the number of uncertainty scenarios (S) for PV generation, wind power, and electricity demand.
Step 4: Set the parameters ε and δ for the probabilistic constraint (32).
Step 5: Set the parameters for FFNN training. Specify the number of hidden units (P), the learning rate, the maximum number of iterations (epochs), and the number of elements in the training, validation, and testing datasets.
Step 6: Set the parameters for the GA, including population size (N), maximum number of generations (B), and the crossover and mutation rates.
Step 7: Generate scenarios using the methodology described in Subsection 3.2.
Step 8: Use an integer random number generator to create the training, testing, and validation datasets needed for FFNN training. Compute the average battery lifetime for each configuration using the energy system model described in Section 2, along with the previously generated scenarios.
Step 9: Using the results from the previous step, apply a training algorithm to the FFNN based on the characteristics defined in Step 5.
Step 10: Using an integer random number generator, create the initial population for the GA based on the parameters from Step 6. Initialize the GA by populating matrix $\boldsymbol{K}$ from equation (48) with N vectors following the structure of equation (47). Each column in $\boldsymbol{K}$ must satisfy the constraints described in Table 1 to ensure feasible individuals.
Step 11: Set the generation index (b) to one ($b \leftarrow 1$) to analyze the first generation.
Step 12: Perform a one-year simulation for each individual $\boldsymbol{k}_{(n)}$ of the population $\boldsymbol{K}$, based on equations (49) and (50), while disregarding the battery aging model. This simulation provides estimates for the fuel consumption of the backup generator and the EIU for each individual $EIU_{(k)}$.
For battery lifetime, evaluate it using the FFNN trained in Step 9 for each system configuration $\boldsymbol{k}_{(n)}$. During this evaluation, if the FFNN produces non-feasible results for battery lifetime, such as negative values, identify the most similar configuration in the training dataset and adopt its lifetime estimation.
Once you have approximated the fuel consumption, EIU, and battery lifetime, calculate the NPC for each individual $NPC_{(k)}$ using the economic parameters from Step 2.
If a particular design $\boldsymbol{k}_{(n)}$ violates the probabilistic constraint (32), assign an arbitrarily high value to its NPC $NPC_{(k)} \leftarrow \infty$. This penalizes and reduces the fitness of those unfeasible individuals.
Step 13: Calculate the fitness $FIT_{(n)}$ of each individual $\boldsymbol{k}_{(n)}$ using equation (51):

$$FIT_{(n)} = \frac{(N+1)-n}{\sum_{\pi=1}^{N}\{(N+1)-\pi\}} \quad \forall\, n = 1, \ldots, N \tag{51}$$

Step 14: Apply the reproduction, crossover, and mutation operators.
Step 15: If $b < B$, set $b \leftarrow b+1$ and proceed to Step 12. Otherwise, stop.

3.3.2. *Integer-coded poplar optimization algorithm*

The POA [35] represents a methodology recently developed, inspired by the propagation mechanisms of poplar trees. This algorithm simulates the process of poplar cuttings and the dispersal of seeds by wind. Furthermore, the POA utilizes historical data and incorporates a

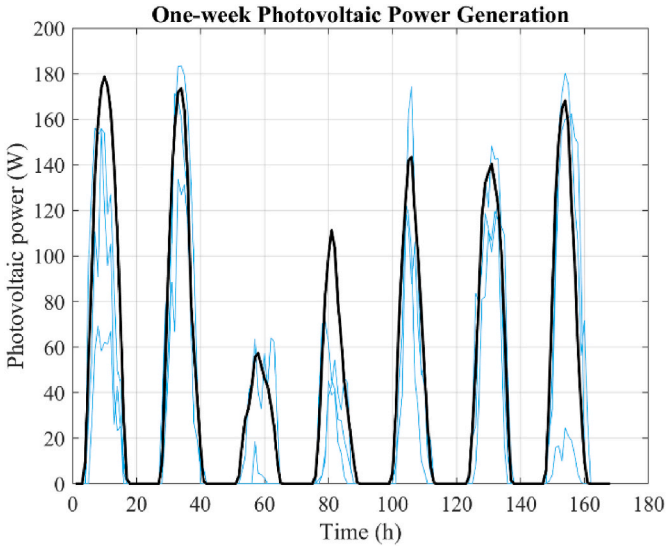

Fig. 8. Scenarios of PV power generation for a 200W panel.

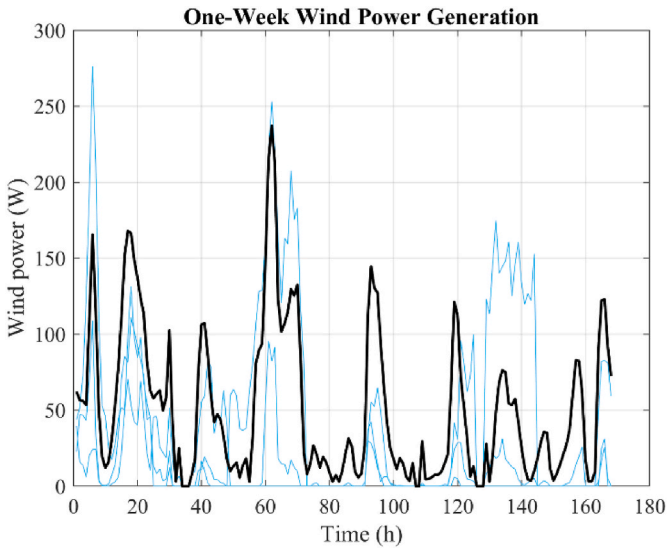

Fig. 9. Scenarios of wind power generation for a 400W turbine.

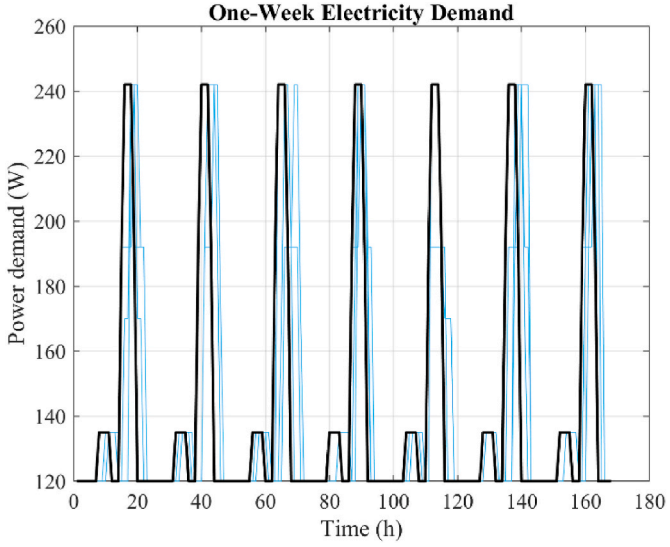

Fig. 10. Scenarios of load demand.

mutation process to enhance the diversity of the solution population. Notably, the POA was originally designed for floating-point number operations. Consequently, in this work, a conversion process from binary to integer variables is employed to adapt the algorithm for specific optimization tasks. Specifically, the operators of POA are initially applied in binary coding, which is subsequently converted to integer coding to calculate the objective function for each individual. The general procedure for implementing the POA is described as follows.

Step 1 Define the dataset of the manufacturers and the available options for the energy system configuration. Create the scenarios of renewable generation and load demand, and set the parameters of the probabilistic constraint. Then, train the FFNN for a fast battery lifetime estimation.
Step 2 Set the parameters δ_{POA}, α_{POA}, and β_{POA} of the POA. Besides, set the population size (N) and maximum number of generations (B). Typical values are $\delta_{POA} = 0.6$, $\alpha_{POA} = 0.6$, and $\beta_{POA} = 1.4$.
Step 3 Using an integer random number generator, create the initial population for the POA based on the parameters from Step 1.
Step 4 Set the generation index (b) to one (b←1) to analyze the first generation.

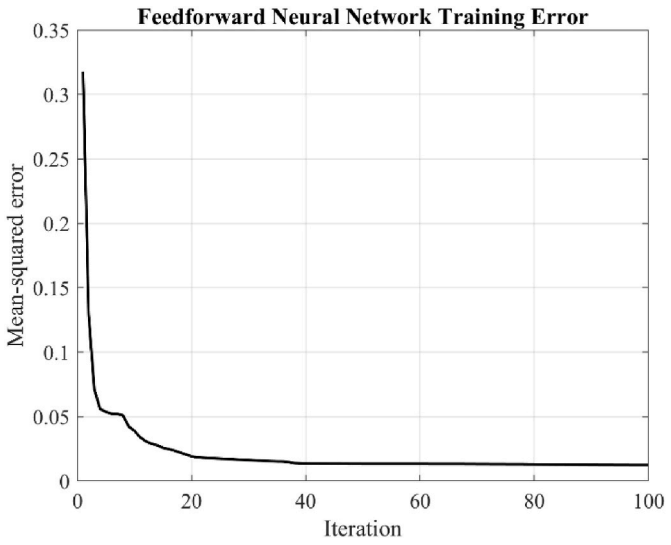

Fig. 11. FFNN training evolution.

Table 11
Results from FFNN training.

Training error	Validation error	Testing error	Monte Carlo trials	Probability of finding a new local optimum
0.0126	0.0163	0.0143	100	0.3

Step 5 Calculate all objective function values of individuals (NPC) and sort them in ascending order. We denote the sorted population as $\boldsymbol{K}_S^{int}$, their individuals as $\boldsymbol{k}_{S(n)}^{int}$, and the corresponding objective-function values as $FIT_{S(n)}$.
Step 6 Convert the integer-coded individuals into binary ones. The resulting population is $\boldsymbol{K}_S^{bin}$ with individuals $\boldsymbol{k}_{(n)}^{bin} \forall\, n = 1, \ldots, N$.
Step 7 Calculate the parameter rr using equation (52):

$$rr = 10 - 8\left[\frac{B-b}{B}\right] \tag{52}$$

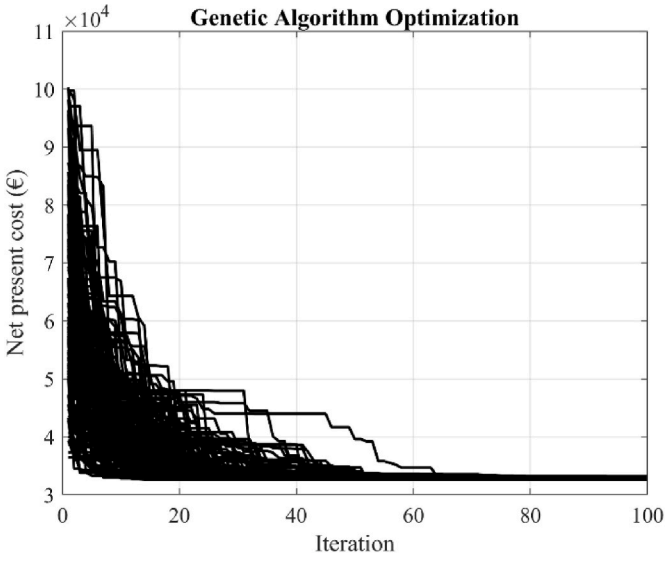

Fig. 12. Genetic algorithm evolution.

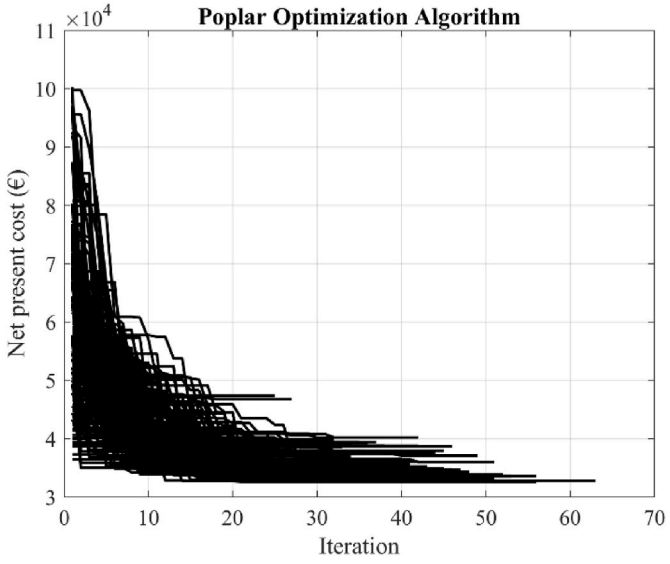

Fig. 13. Poplar optimization algorithm evolution.

Step 8 Calculate the chaos factor for the first portion of the sorted population and the next iteration ($F_{CH(n)}$) according to equation (53):

$$F_{CH(n)} \leftarrow \mu_{POA} \times F_{CH(n)} \left(1 - F_{CH(n)}\right) \; \forall \; n = 1, \ldots, floor(\delta_{POA} \times N), \tag{53}$$

where the parameter μ_{POA} is set to a typical value of 4.

Step 9 Calculate the height ($H_{POA(n)}$) using equation (54):

$$H_{POA(n)} = \alpha_{POA} H_{max} \left(\frac{1/FIT_{S(n)}}{\sum_{\pi}^{floor(\delta_{POA} N)} 1/FIT_{S(\pi)} + \varepsilon_{POA}} \right) \tag{54}$$
$$\forall \; n = 1, \ldots, floor(\delta_{POA} \times N)$$

where the parameter ε_{POA} is a small tolerance, and H_{max} is set to one since the binary coding is used.

Step 10 Update the position of each individual using equation (55):

$$k^{bin}_{(n,\sigma)} \leftarrow k^{bin}_{(n,\sigma)} + r_1 H_{POA(n)} \; tan\left(\frac{\pi}{rr} r_2\right) \left(1 + F_{CH(n)} \; cos(r_3 \pi)\right) \tag{55}$$

where the index σ refers to each element of the vector $\boldsymbol{k}^{bin}_{(n)}$. It is essential to highlight that the elements of the vector $\boldsymbol{k}^{bin}_{(n)}$ depends on the number of bits required to represent the associated magnitudes or, in other words, the maximum value between *V*, *D*, *Z*, *J*, *M*, *O*, and *Y*. The factors r_1 and r_3 are random numbers in interval [0,1], and r_2 is a random in the interval [-1,1].

Step 11 The results of Step 10 for $k^{bin}_{(n,\sigma)}$ will be floating point numbers that need to be converted into binaries. Thus, depending on the value of $k^{bin}_{(n,\sigma)}$ obtained from equation (55), we will select the closest among zero or one.

Step 12 Convert the binary-coded individuals $\boldsymbol{k}^{bin}_{(n)}$ to integers ($\boldsymbol{k}^{int}_{(n)}$) and limit them to a feasible interval as specified in Table 1.

Table 13
Results from FFNN training.

Optimization Method	Probability of finding a new local optimum
GA	0.0150
POA	0.0800

Step 13 Calculate the objective function value for the individuals obtained in Step 12 ($\boldsymbol{k}^{int}_{(n)}$). Then, these individuals are sequentially compared with the first $floor(\delta_{POA} \times N)$ agents of the population $\boldsymbol{K}^{int}_{S}$ of Step 5. From this comparison, we select those with the best fitness.

Step 14 Initialize the historical population ($\boldsymbol{K}^{hist}_{S}$) using the binary-coded population of Step 6. In other words, set $\boldsymbol{K}^{hist}_{S} \leftarrow \boldsymbol{K}^{bin}_{S}$. Repeat this procedure for the fitness vector of the historical population ($FIT_{hist(n)}$). Set $FIT_{hist(n)} \leftarrow FIT_{S(n)}$.

Step 15 Permute the position of the individuals of the historical population ($\boldsymbol{K}^{hist}_{S}$) if a random condition is fulfilled. To this end, two uniform random numbers are compared to decide whether the members of the historical population are to be shuffled.

Step 16 Consider the individuals $n = floor(\delta_{POA} \times N) + 1, \ldots, N$. For each value of n randomly select another individual (kk) from the historical population. Then, calculate the coefficient C_{POA} using equation (56):

$$C_{POA} = \frac{FIT_{bst}}{FIT_{bst} + FIT_{hist(kk)}} \tag{56}$$

where FIT_{bst} is the fitness of the best individual and $FIT_{hist(kk)}$ is the fitness of the agent kk of the historical population.

Step 17 Update the position of each individual using equation (57):

$$k^{bin}_{(n,\sigma)} \leftarrow k^{bin}_{(kk,\sigma)} + (1 - C_{POA}) \left(k_{bst(\sigma)} - k^{bin}_{(n,\sigma)}\right) + C_{POA} \left(k^{hist}_{(kk,\sigma)} - k^{hist}_{(k,\sigma)}\right) \tag{57}$$

Step 18 The results of Step 17 for $k^{bin}_{(n,\sigma)}$ will be floating point numbers that need to be converted into binaries. Thus, depending on the value of $k^{bin}_{(n,\sigma)}$ obtained from equation (57), we will select the closest among zero or one.

Step 19 Convert the binary-coded individuals $\boldsymbol{k}^{bin}_{(n)}$ to integers ($\boldsymbol{k}^{int}_{(n)}$) and limit them to a feasible interval as specified in Table 1.

Step 20 Calculate the objective function value for the individuals obtained in Step 19 ($\boldsymbol{k}^{int}_{(n)}$). Then, these individuals are sequentially compared with those in the population $\boldsymbol{K}^{int}_{S}$ of Step 5. From this comparison, we select those with the best fitness.

Step 21 Create an improved population by concatenating the results of Step 13 with those obtained in Step 20 (binary-coded individuals). Then, this population will be sorted according to fitness in ascending order.

Step 22 Apply the mutation operator of equation (58) to the population obtained in Step 21. The operator is applied to the elements with relatively low performance ($n = floor(\delta_{POA} \times N) + 1, \ldots, N$).

$$k^{bin}_{(n,\sigma)} \leftarrow k^{bin}_{(n,\sigma)} + \beta_{POA} r_4 \left(k^{hist}_{(n,\sigma)} - k^{bin}_{(n,\sigma)}\right) \tag{58}$$

Step 23 Convert the binary-coded individuals $\boldsymbol{k}^{bin}_{(n)}$ to integers ($\boldsymbol{k}^{int}_{(n)}$) and limit them to a feasible interval as specified in Table 1.

Table 12
Optimal energy system configuration.

Solar panel type (*v*)	Panels in parallel (*d*)	Wind turbine type (*z*)	Wind turbines (*j*)	Battery type (*m*)	Batteries in parallel (*o*)	Generator type (*y*)
21 (555 W)	6	4 (1000 W)	1	4 (600 Ah)	1	1 (0 W)

Step 24 Calculate the objective function value for the individuals obtained in Step 23 ($k_{(n)}^{int}$). Then, these individuals are sequentially compared with those obtained in Step 21. From this comparison, we select those with the best fitness.

The methodology presented in this work is summarized in Fig. 7.

4. Case study

The technique proposed in this work for optimally designing a hybrid energy system under uncertainty is demonstrated using a hypothetical case study in the Manicaland province of Zimbabwe (latitude −19.0188°, longitude 32.3689°). The subsequent section provides a detailed overview of the conditions considered.

4.1. Case description

The system under study is designed to provide energy to a small residential system equipped with a water pump. A typical nominal voltage of 24 V has been chosen. The load demand consists of four devices ($l = 1, 2, 3, L = 4$). Each device has its power demand $P_{D(l)}$, operating hours $\Delta h_{(l)}$, and is operational between times $h_{(l)}^{min}$ and $h_{(l)}^{max}$, as detailed in Table 2. Device 1 ($l = 1$) acts as a base load. Meanwhile, Device 2 ($l = 2$) is a water pump meant to run for 5 h ($\Delta h_{(2)} = 5$) at any time between hour 1 ($h_{(2)}^{min} = 1$) and 24 ($h_{(2)}^{max} = 2$).

The list of considered PV panel manufacturers ($v = 2, \ldots, V$) is presented in Table 3. This table includes the rated power $P_{STC(v)}$, temperature coefficient $\alpha_{PV(v)}$, nominal operating cell temperature $NOTC_{(v)}$, and capital cost for each manufacturer. Replacement costs are assumed to be equal to capital costs, and operation and maintenance (O&M) charges are not taken into account. The index for PV panel manufacturers (v) in Table 3 starts from 2 because $v = 1$ represents a configuration without a PV generator.

The list of wind turbine manufacturers ($z = 2, \ldots, Z$) can be found in Table 4, which displays both the rated capacity and capital cost. As with the previous section, replacement costs are set to match capital expenses. O&M costs are assumed to be 2 % of the capital expenses annually. As previously noted, the index $z = 1$ indicates a system configuration without wind generation.

The list of backup generators ($y = 2, \ldots, Y$) can be found in Table 5. They are all presumed to use gasoline as fuel, with a lifetime of 750 h and O&M costs of 0.25 €/h. For fuel consumption estimation, we have used the typical consumption curves usually provided by manufacturers. As noted earlier, the index $y = 1$ indicates a system configuration without conventional generation.

The list of battery manufacturers ($m = 2, \ldots, M$) examined in this study is detailed in Table 6. This table presents the 10-h capacity $C_{10(m)}$, number of operational cycles $Z_{I(m)}$, minimum SOC $SOC_{BT(m)}^{MIN}$, float lifetime $FL_{(m)}$, and capital costs. All batteries are of the OGi type. The index $m = 1$ denotes an energy system without LABs. Replacement costs are set to match the capital costs, and O&M costs have been disregarded.

Table 7 showcases the techno-economic parameters pertinent to NPC cost estimation. As previously mentioned in Sub-section 3.3, the technique utilized in this study leverages a surrogate model of the behavior of the system to gauge the associated battery lifetime. This surrogate model is underpinned by an FFNN (as depicted in Fig. 6), which was trained employing the Levenberg–Marquardt algorithm based on parameters laid out in Table 8. The comprehensive dataset used for FFNN training consists of 12500 points. Out of this dataset, 80 % is allocated for training, 10 % for validation, and the remaining 10 % for testing.

Uncertainty in FFNN training was addressed using the MCS approach. Specifically, the training process was executed multiple times (100 experiments) from distinct random starting points (RSPs). This method enables the identification of local minima with a certain probability. Further details are provided in Refs. [49,50].

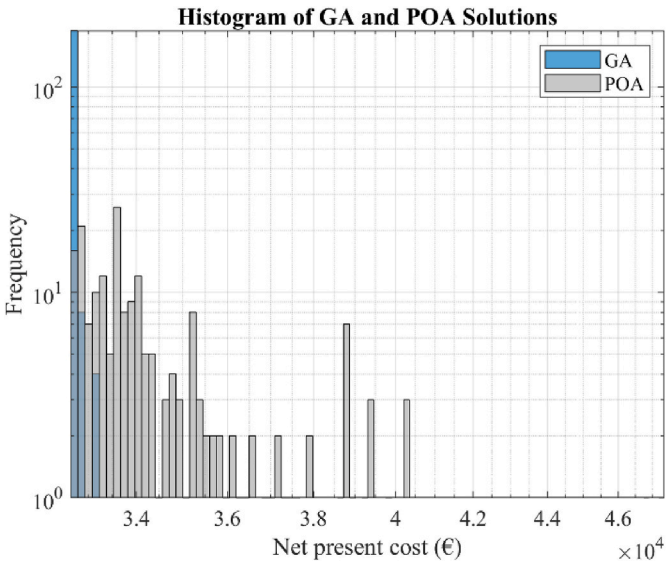

Fig. 14. Histogram of local optima.

After the FFNN is trained, the integer-coded GA and POA are executed using the parameters and specifications outlined in Tables 9 and 10, requiring an EIU and a confidence interval equal to 1 %.

Following the same procedure applied to the FFNN training, the GA and POA are sequentially repeated starting from different RSPs to identify diverse local minima. Subsequently, the probability of discovering a new local minimum by extending the random search is calculated as the ratio of the number of singleton domains discovered to the total number of experiments conducted through Monte Carlo simulations. Here, singleton domains are defined as those solutions that are identified uniquely by a single RSP. This methodology was employed in

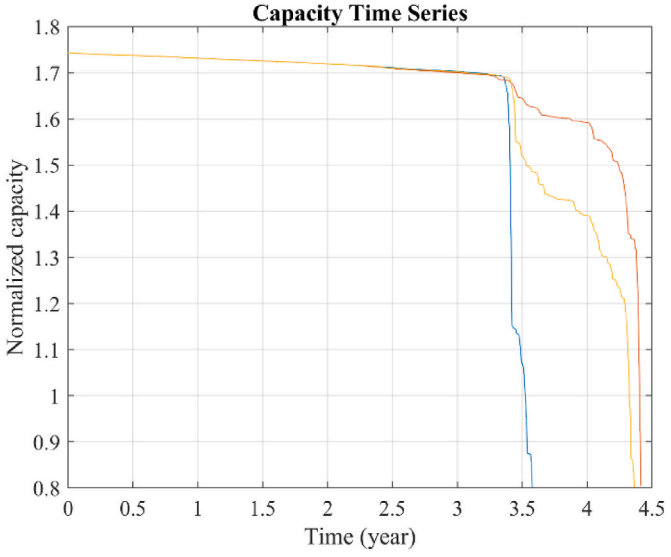

Fig. 15. Normalized capacity time series.

200 instances (200 Monte Carlo simulations or RSPs) to ascertain the optimal design utilizing both a GA and a POA. In the context of the GA, the optimization process was undertaken over 100 iterations (where B equals 100). Conversely, for the POA, the optimization process was terminated if no modifications were observed following 10 iterations, up to a maximum of 100 iterations. This criterion was established because

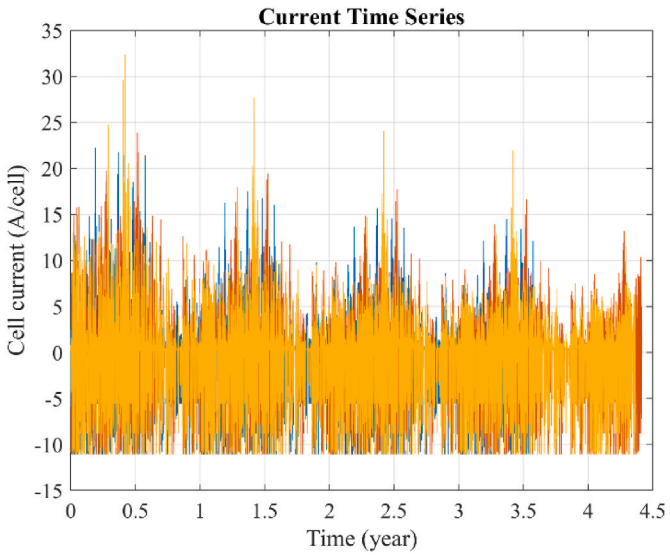

Fig. 16. Battery current time series.

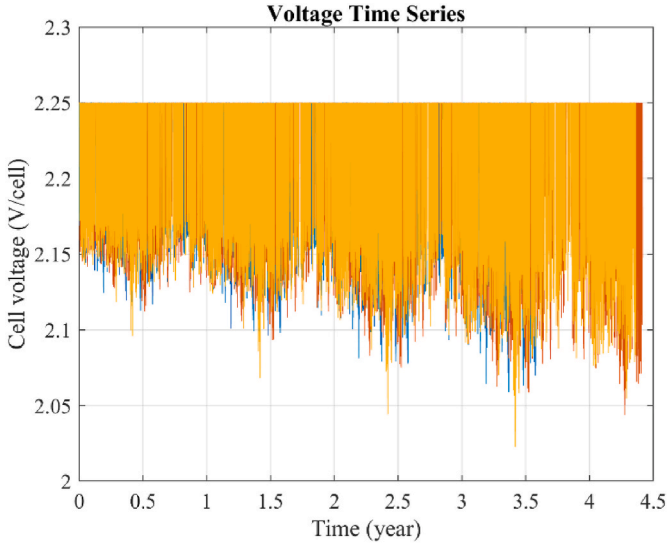

Fig. 17. Battery voltage time series.

the POA necessitates a greater number of objective function evaluations compared to the GA.

4.2. Results and discussions

Results derived from the energy system model detailed in Section 2 are presented here. These results, essential for implementing the methodology discussed in Section 3, are based on parameters and conditions described in Sub-section 4.1.

The presentation begins with calculations tied to the scenario generation process. This is followed by details of the FFNN training. We then transition into showcasing the results of the dimensioning procedure, concluding with the outcomes of a probabilistic simulation.

The technique was executed in MATLAB® on a PC 433, boasting an Intel Core® i7 CPU, 16 GB RAM, and a 64-bit operating system. For the implementation of the weighted Ah throughput model, LAB parameters are available in Refs. [38–40]. Parameters for power converter modeling can be referenced in Ref. [41].

Renewable power generation uncertainty is represented using 3 scenarios ($S = 3$). Fig. 8 visualizes the initial 168 h of PV generation for the first manufacturer listed in Table 3 (200 W), including the primary

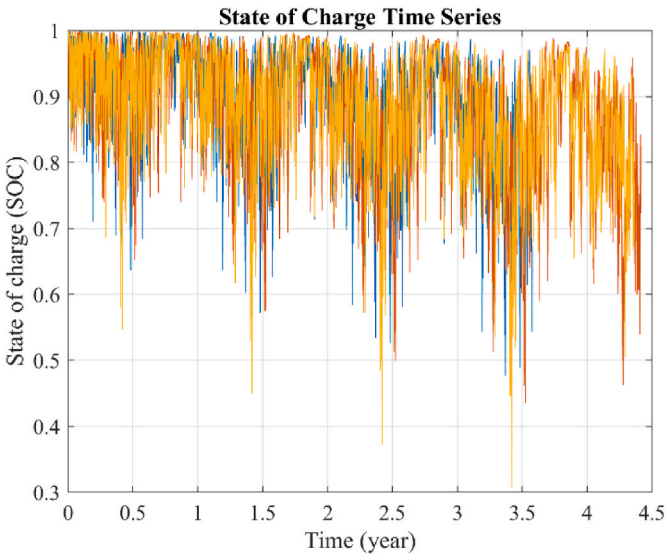

Fig. 18. SOC time series.

generation profile from which scenarios were generated. Similarly, Fig. 9 illustrates wind generation scenarios for the first manufacturer in Table 4 (400 W), highlighting the pronounced effects of increased uncertainty on the crafted scenarios. Fig. 10 captures the inaugural week of load demand scenarios, formulated using data from Table 2. For clarity, only the first week is plotted, though it should be noted this represents the starting week in an annual scenario generation methodology.

Fig. 11 illustrates the progression (lowest error in 100 RSPs) of the FFNN training process based on the configurations and structure outlined in Table 8. The validation and testing errors are detailed in Table 11, providing further context to this result. As previously noted, the FFNN training is conducted using the Levenberg–Marquardt algorithm, starting from various RSPs. This approach helps circumvent stagnation around local minima. After identifying these local minima, we assessed the likelihood of discovering a new one upon repeating the training experiment. The calculated probability is documented in Table 11. These findings suggest a reasonable confidence level that the trained FFNN achieved minimal error. An in-depth discussion of the utilized methodology is available in Ref. [50].

The progression of the optimization process is depicted in Fig. 12 for the GA and Fig. 13 for the POA, with the attributes of the system detailed in Table 12. Notably, the optimal configuration does not include a backup generator, indicating that the energy demand is met exclusively through a combination of renewable power sources and the LAB.

The search for the global minimum using the GA and the POA resulted in the identification of the same system configuration, as described in Table 12. In Fig. 12, we observe that the GA reached local minima very close to each other. On the other hand, Fig. 13 illustrates how the POA reached different local minima, influenced by the stopping criterion applied to this method. This behavior significantly influences the estimation of the probability of finding a new local optimum, which

Table 14
Energy system performance using FFNN.

Net present cost (€)	Energy index of unreliability (%)	Battery lifetime (year)
32631	0	5.1853

Table 15
Energy system performance using weighted Ah throughput model.

Net present cost (€)	Energy index of unreliability (%)	Battery lifetime (year)
36101	0	4.1193

Table 16
Optimal energy system configuration without uncertainty.

Solar panel type (v)	Panels in parallel (d)	Wind turbine type (z)	Wind turbines (j)	Battery type (m)	Batteries in parallel (o)	Generator type (y)
15 (540 W)	4	5 (1800 W)	1	2 (200 Ah)	1	1 (0 W)

Table 17
System performance using weighted Ah throughput model without uncertainty.

Net present cost (€)	Energy index of unreliability (%)	Battery lifetime (yr)
26820	0	9.06

is reported in Table 13 for each method.

Fig. 14 displays the local minima reached by each method. We observe that the number of local minima at which the POA stagnates exceeds that of the GA. This accounts for the higher probability of finding a new solution as reported in Table 13. It is crucial to emphasize that a low probability of discovering a new local minimum implies a higher likelihood that the identified local minimum is, in fact, global. This is because the probability of finding a new solution is inversely related to the number of RSPs. Enhancing the search process by increasing the number of RSPs necessitates additional computational time.

The optimal design, outlined in Table 12, has been evaluated using the respective scenarios for PV, wind, and load demand. Figs. 15–18 display pertinent simulation outcomes: battery capacity in Fig. 15, cell current in Fig. 16, cell voltage in Fig. 17, and battery SOC in Fig. 18. As inferred from Fig. 15, there is a marked progression of aging processes in the LAB. These processes appear consistent across scenarios within the initial three years but diverge significantly thereafter. Figs. 16 and 17 highlight a diminished LAB charge acceptance attributable to aging mechanisms and their consequential impact on battery voltage. Lastly, Fig. 18 underscores the challenges faced by the LAB in achieving a high SOC as it nears the end of its operational lifespan.

As an extension to the results presented in Fig. 15, the lifetime of the battery is estimated to be between 3.58 and 4.42 years, with an average of 4.12 years. Furthermore, the NPC estimations vary between 34861 € and 38398 €, with an average of 36101 €. The EIU is anticipated to be zero, indicating that the energy demand would be fully satisfied.

Utilizing a surrogate energy system model to estimate battery lifetime inherently introduces some degree of error. Tables 14 and 15 present comparative results between the evaluation conducted using the FFNN and the weighted Ah throughput model to assess this error. These comparisons indicate that the discrepancies in estimating the NPC and battery lifetime amount to 9.6 % and 20.6 %, respectively.

Regarding the EIU estimation, it is crucial to note that the approach proposed in this study does not account for variations in internal resistances over time, as demonstrated in references (49) and (50). These variations directly influence our ability to simulate the charge acceptance of the battery, which, in turn, affects the calculation of the EIU. This limitation could diminish the accuracy of the EIU estimation.

Many commercial tools commonly employ deterministic optimization for the design of energy systems. Thus, comparing the outcomes from probabilistic and deterministic methods can offer a more comprehensive understanding of the approach introduced in this study. For this purpose, we utilized the same integer-coded GA with the TMY time series, thereby eliminating any uncertainties associated with renewable power generation. Table 16 presents the optimal system configuration, whereas Table 17 provides details on the NPC, EIU, and battery lifetime. Upon comparing the NPC estimation from Table 15 with that in Table 17, a discrepancy of 25.7 % is observed. The probabilistic approach advocates for a system configuration with increased PV generation and storage capacity but reduced wind generation. Furthermore, in the absence of uncertainty, the renewable generation profile yields a more favorable outlook, wherein the LAB lifetime is extended to 9.06 years, substantially lowering the NPC estimate. It is crucial to acknowledge that during the scenario generation process, the profile representing TMY behavior is not among the considered scenarios; this omission is evident as the scenario does not manifest in Fig. 15.

Table 18
Computational time for probabilistic and deterministic optimization.

Scenario generation (hh:mm:ss)	FFNN training (hh:mm:ss)	Probabilistic GA (hh:mm:ss)	Probabilistic POA (hh:mm:ss)	Deterministic GA (hh:mm:ss)
00:00:06	00:01:30	19:03:33	24:54:59	0:10:38

Another point of interest pertains to the computational burden. Table 18 displays the duration required for scenario generation, FFNN training, and optimization utilizing both the GA and the POA. Additionally, the time taken for deterministic optimization is also documented.

It is crucial to recognize that the time required to compile the dataset increases directly in proportion to its size. The approach through which the FFNN is implemented—outside the optimization process—proves beneficial. This separation allows for the estimation of battery lifetime using multi-year simulations independently from the optimization process. Furthermore, probabilistic optimization necessitates more time than its deterministic counterpart, attributed to the additional simulations required for the EIU estimation, as outlined in equations (49) and (50). In accordance with the implementation of the GA and the POA conducted in this study, it was observed that the POA required approximately 31.6 % more time than the GA.

5. Conclusions

This work presented an optimization model for dimensioning hybrid energy systems under uncertainty, leveraging stochastic optimization theory. Initially, scenarios for PV, wind generation, and electricity demand were generated using the TMY data and its associated uncertainty. The TMY time series, sourced from Renewables.ninja, were integrated with an uncertainty measure as discussed. Subsequently, a database detailing energy system configurations was constructed. This database was then simulated to estimate the LAB lifetime using the weighted Ah throughput model, necessitating a multi-year simulation. However, system reliability, as measured by the EIU, was evaluated using just a single-year simulation. This strategy effectively separates the LAB lifetime computation from the main optimization process, thereby enhancing computational efficiency. Put succinctly, the proposed approach eliminates the need for multi-year energy system simulation during optimization by utilizing an FFNN.

The implications of the proposed technique were evaluated through a hypothetical case study. Introducing a surrogate model based on an FFNN resulted in an approximation error of 9.6 % for the NPC estimation and 20.6 % for the LAB lifetime estimation. When comparing the proposed probabilistic technique with its deterministic counterpart, the probabilistic design suggests an energy system with an NPC that is 25.7 % higher than what the deterministic approach yields. The probability of finding a new solution by repeating the optimization routine (200 Monte Carlo experiments) from a different random point was 1.5 % for the GA and 8 % for the POA. The POA was able to find more local minima due to the characteristics of its operators and the stopping criterion implemented.

Potential directions for future research include the adoption of

parallel computing technologies.

CRediT authorship contribution statement

Juan M. Lujano-Rojas: Conceptualization. **Rodolfo Dufo-López:** Funding acquisition. **Jesús Sergio Artal-Sevil:** Validation. **Eduardo García-Paricio:** Supervision.

Declaration of generative AI and AI-assisted technologies in the writing process

During the preparation of this work the authors used ChatGPT-4 in order to improve the language and readability of the manuscript. After using this service, the author reviewed and edited the content as needed and take full responsibility for the content of the publication.

Declaration of competing interest

The authors declare the following financial interests/personal relationships which may be considered as potential competing interests:

Rodolfo Dufo-Lopez reports financial support was provided by Spanish Government (Ministerio de Ciencia e Innovación, Agencia Estatal de Investigación). Rodolfo Dufo-Lopez reports financial support was provided by European Regional Development Fund. If there are other authors, they declare that they have no known competing financial interests or personal relationships that could have appeared to influence the work reported in this paper.

Acknowledgment

This work was supported by the Spanish Government (Ministerio de Ciencia e Innovación, Agencia Estatal de Investigación) and by the European Union/European Regional Development Fund [Grant PID2021-123172OB-I00 funded by MCIN/AEI/10.13039/501100011033 and by "ERDF A way of making Europe"]; [Grant TED2021-129801B–I00 funded by MCIN/AEI/10.13039/501100011033 and by European Union NextGenerationEU/PRTR].

References

[1] P. Roy, J. He, T. Zhao, Y.V. Singh, Recent advances of wind-solar hybrid renewable energy systems for power generation: a review, IEEE Open Journal of the Industrial Electronics Society 3 (2022) 81–104, https://doi.org/10.1109/OJIES.2022.3144093.

[2] A.K. Onaolapo, G. Sharma, P.N. Bokoro, T. Adefarati, R.C. Bansal, A comprehensive review of the design and operations of a sustainable hybrid power system, Comput. Electr. Eng. 111 (A) (2023) 108954, https://doi.org/10.1016/j.compeleceng.2023.108954.

[3] M. Jasinski, A. Najafi, O. Homaee, M. Kermani, G. Tsaousoglou, Z. Leonowicz, T. Novak, Operation and planning of energy hubs under uncertainty—a review of mathematical optimization approaches, IEEE Access 11 (2023) 7208–7228, https://doi.org/10.1109/ACCESS.2023.3237649.

[4] O.L. Oyewole, N.I. Nwulu, E.J. Okampo, Optimal design of hydrogen-based storage with a hybrid renewable energy system considering economic and environmental uncertainties, Energy Convers. Manag. 300 (2024) 117991, https://doi.org/10.1016/j.enconman.2023.117991.

[5] I.F. Davoudkhani, A. Dejamkhooy, S.A. Nowdeh, A novel cloud-based framework for optimal design of stand-alone hybrid renewable energy system considering uncertainty and battery aging, Appl. Energy 344 (2023) 121257, https://doi.org/10.1016/j.apenergy.2023.121257.

[6] S.W. Jin, Y.P. Li, Analyzing the performance of electricity, heating, and cooling supply nexus in a hybrid energy system of airport under uncertainty, Energy 272 (2023) 127138, https://doi.org/10.1016/j.energy.2023.127138.

[7] T. Yuan, Y. Mu, T. Wang, Z. Liu, A. Pirouzi, Using firefly algorithm to optimally size a hybrid renewable energy system constrained by battery degradation and considering uncertainties of power sources and loads, Heliyon (2024) e26961, https://doi.org/10.1016/j.heliyon.2024.e26961.

[8] M. Gopila, G. Suresh, D. Prasad, Random decision forest (RDF) and crystal structure algorithm (CryStAl) for uncertainty consideration of RES & load demands with optimal design of hybrid CCHP systems, Energy 282 (2023) 128545, https://doi.org/10.1016/j.energy.2023.128545.

[9] M. Yadegari, H. Sahebi, S. Razm, J. Ashayeri, A sustainable multi-objective optimization model for the design of hybrid power supply networks under uncertainty, Renew. Energy 219 (2023) 119443, https://doi.org/10.1016/j.renene.2023.119443.

[10] S.A. Nowdeh, A. Naderipour, I.F. Davoudkhani, J.M. Guerrero, Stochastic optimization – based economic design for a hybrid sustainable system of wind turbine, combined heat, and power generation, and electric and thermal storages considering uncertainty: a case study of Espoo, Finland, Renew. Sustain. Energy Rev. 183 (2023) 113440, https://doi.org/10.1016/j.rser.2023.113440.

[11] F.G. Li, S.J. Chen, C.Q. Ju, X.S. Zhang, G.W. Ma, W.B. Huang, Research on short-term joint optimization scheduling strategy for hydro-wind-solar hybrid systems considering uncertainty in renewable energy generation, Energy Strategy Rev. 101242 (2023), https://doi.org/10.1016/j.esr.2023.101242.

[12] K.X. Lei, J.X. Chang, X.B. Wang, A.J. Guo, Y.M. Wang, C.Q. Ren, Peak shaving and short-term economic operation of hydro-wind-PV hybrid system considering the uncertainty of wind and PV power, Renew. Energy 215 (2023) 118903, https://doi.org/10.1016/j.renene.2023.118903.

[13] Y.C. Dong, H.L. Zhang, P. Ma, C. Wang, X.J. Zhou, A hybrid robust-interval optimization approach for integrated energy systems planning under uncertainties, Energy 274 (2023) 127267, https://doi.org/10.1016/j.energy.2023.127267.

[14] G. Furlan, F. You, Robust design of hybrid solar power systems: sustainable integration of concentrated solar power and photovoltaic technologies, Advances in Applied Energy 13 (2024) 100164, https://doi.org/10.1016/j.adapen.2024.100164.

[15] A. Bamshad, O. Safarzadeh, Uncertainty and sensitivity analysis of generation expansion planning in hybrid nuclear and renewable energy system, Prog. Nucl. Energy 163 (2023) 104812, https://doi.org/10.1016/j.pnucene.2023.104812.

[16] Z.U. Rizqi, S.Y. Chou, T.H.K. Yu, Green energy mix modeling under supply uncertainty: hybrid system dynamics and adaptive PSO approach, Appl. Energy 349 (2023) 121643, https://doi.org/10.1016/j.apenergy.2023.121643.

[17] S. Divya, M.K. Paramathma, A. Sheela, S.D. Kumar, Hybrid renewable energy source optimization using black widow optimization techniques with uncertainty constraints, Measurement: Sensors 31 (2024) 100968, https://doi.org/10.1016/j.measen.2023.100968.

[18] Y.T. Wang, X.Y. Ji, Optimization model for low-carbon supply chain considering multi-level backup strategy under hybrid uncertainty, Appl. Math. Model. 126 (2023) 1–21, https://doi.org/10.1016/j.apm.2023.10.034.

[19] S.J.H. Dehshiri, M. Amiri, Considering the circular economy for designing closed-loop supply chain under hybrid uncertainty: a robust scenario-based possibilistic-stochastic programming, Expert Syst. Appl. (2024) 121745, https://doi.org/10.1016/j.eswa.2023.121745.

[20] G. Er, G. Soykan, E. Canakoglu, Stochastic optimal design of a rural microgrid with hybrid storage system including hydrogen and electric cars using vehicle-to-grid technology, J. Energy Storage 75 (2024) 109747, https://doi.org/10.1016/j.est.2023.109747.

[21] Z.F. Liu, S.X. Zhao, S.L. Zhao, G.D. You, X.X. Hou, J.L. Yu, L.L. Li, B. Chen, Improving the economic and environmental benefits of the energy system: a novel hybrid economic emission dispatch considering clean energy power uncertainty, Energy 285 (2023) 128668, https://doi.org/10.1016/j.energy.2023.128668.

[22] S. Bhavsar, R. Pitchumani, M.A. Ortega-Vazquez, N. Costilla-Enriquez, A hybrid data-driven and model-based approach for computationally efficient stochastic unit commitment and economic dispatch under wind and solar uncertainty, Int. J. Electr. Power Energy Syst. 151 (2023) 109144, https://doi.org/10.1016/j.ijepes.2023.109144.

[23] S. Kim, Y. Choi, J. Park, D. Adams, S. Heo, J.H. Lee, Multi-period, multi-timescale stochastic optimization model for simultaneous capacity investment and energy management decisions for hybrid Micro-Grids with green hydrogen production under uncertainty, Renew. Sustain. Energy Rev. 190 (2024) A, https://doi.org/10.1016/j.rser.2023.114049.

[24] N. Belbachír, S. Kamel, M.H. Hassan, M. Zellagui, Optimizing energy management of hybrid wind generation-battery energy storage units with long-term memory artificial hummingbird algorithm under daily load-source uncertainties in electrical networks, J. Energy Storage 78 (2024) 110288, https://doi.org/10.1016/j.est.2023.110288.

[25] C. Yan, Y. Zou, Z. Wu, A. Maleki, Effect of various design configurations and operating conditions for optimization of a wind/solar/hydrogen/fuel cell hybrid microgrid system by a bio-inspired algorithm, Int. J. Hydrogen Energy 60 (2024) 378–391, https://doi.org/10.1016/j.ijhydene.2024.02.004.

[26] I.E. Atawi, A. Abuelrub, A.Q. Al-Shetwi, O.H. Albalawi, Design of a wind-PV system integrated with a hybrid energy storage system considering economic and reliability assessment, J. Energy Storage 81 (2024) 110405, https://doi.org/10.1016/j.est.2023.110405.

[27] Y. Liu, M. Peng, Research on peak load shifting for hybrid energy system with wind power and energy storage based on situation awareness, J. Energy Storage 82 (2024) 110472, https://doi.org/10.1016/j.est.2024.110472.

[28] Z.M. Guan, C.Y. Lu, Y.M. Li, J.J. Wang, Chance-constrained optimization of hybrid solar combined cooling, heating and power system considering energetic, economic, environmental, and flexible performances, Renew. Energy 212 (2023) 908–920, https://doi.org/10.1016/j.renene.2023.05.084.

[29] F. Mottola, D. Proto, A. Russo, Probabilistic planning of a battery energy storage system in a hybrid microgrid based on the Taguchi arrays, Int. J. Electr. Power Energy Syst. 157 (2024) 109886, https://doi.org/10.1016/j.ijepes.2024.109886.

[30] S. Mohseni, A.C. Brent, Probabilistic sizing and scheduling co-optimisation of hybrid battery/super-capacitor energy storage systems in micro-grids, J. Energy Storage 73 (D) (2023) 109172, https://doi.org/10.1016/j.est.2023.109172.

[31] G.Y. Zhu, G.G. Yan, D. Garmroudi, Optimizing solar-wind hybrid energy systems for sustainable charging stations and commercial applications: a two-stage

framework with ebola-inspired optimization, Expert Syst. Appl. 246 (2024) 123180, https://doi.org/10.1016/j.eswa.2024.123180.
[32] H. Haghighat, W. Wang, B. Zeng, Robust microgrid capacity investment with endogenous and exogenous uncertainties, IEEE Trans. Smart Grid (2024), https://doi.org/10.1109/TSG.2023.3326834.
[33] M. Billah, M. Yousif, M. Numan, I.U. Salam, S.A.A. Kazmi, T.A.H. Alghamdi, Decentralized smart energy management in hybrid microgrids: evaluating operational modes, resources optimization, and environmental impacts, IEEE Access 11 (2023) 143530–143548, https://doi.org/10.1109/ACCESS.2023.3343466.
[34] Renewables.ninja. https://www.renewables.ninja/, 2023. (Accessed 23 October 2023).
[35] D. Chen, Y. Ge, Y. Wan, Y. Deng, Y. Chen, F. Zou, Poplar optimization algorithm: a new meta-heuristic optimization technique for numerical optimization and image segmentation, Expert Syst. Appl. 200 (2022) 117118, https://doi.org/10.1016/j.eswa.2022.117118.
[36] A.C. Jimenez, K. Olson, Renewable energy for rural health clinics. U.S. National Renewable Energy Laboratory, (1998). https://www.nrel.gov/docs/fy99osti/26224.pdf.
[37] T. Lambert, P. Gilman, P. Lilienthal, Micropower system modeling with Homer, in: F.A. Farret, S.M. Godoy (Eds.), Integration of Alternative Sources of Energy, John Wiley & Sons, Inc, Hoboken, New Jersey, 2006, pp. 379–418.
[38] J. Schiffer, D.U. Sauer, H. Bindner, T. Cronin, P. Lundsager, R. Kaiser, Model prediction for ranking lead-acid batteries according to expected lifetime in renewable energy systems and autonomous power-supply systems, J. Power Sources 168 (1) (2007) 66–78, https://doi.org/10.1016/j.jpowsour.2006.11.092.
[39] A. Andersson, Battery Lifetime Modelling, Denmark National Laboratory Risø, 2006. https://docplayer.net/7879566-Battery-lifetime-modelling.html.
[40] H. Bindner, T. Cronin, P. Lundsager, J.F. Manwell, U. Abdulwahid, I. Baring-Gould, Lifetime Modelling of Lead Acid Batteries, Denmark National Laboratory Risø, 2005. https://www.osti.gov/etdeweb/servlets/purl/20607163.
[41] G.A. Rampinelli, A. Krenzinger, F.C. Romero, Mathematical models for efficiency of inverters used in grid connected photovoltaic systems, Renew. Sustain. Energy Rev. 34 (2014) 578–587, https://doi.org/10.1016/j.rser.2014.03.047.
[42] V.S. Pappala, I. Erlich, K. Rohrig, J. Dobschinski, A stochastic model for the optimal operation of a wind-thermal power system, IEEE Trans. Power Syst. 24 (2) (2009) 940–950, https://doi.org/10.1109/TPWRS.2009.2016504.
[43] S. Pfenninger, I. Staffell, Long-term patterns of European PV output using 30 years of validated hourly reanalysis and satellite data, Energy 114 (2016) 1251–1265, https://doi.org/10.1016/j.energy.2016.08.060.
[44] I. Staffell, S. Pfenninger, Using bias-corrected reanalysis to simulate current and future wind power output, Energy 114 (2016) 1224–1239, https://doi.org/10.1016/j.energy.2016.08.068.
[45] M.M. Ortiz, L. Kvalbein, L. Hellemo, Evaluation of open photovoltaic and wind production time series for Norwegian locations, Energy 236 (2021) 121409, https://doi.org/10.1016/j.energy.2021.121409.
[46] Generating synthetic wind data. https://www.homerenergy.com/products/pro/docs/3.9/generating_synthetic_wind_data.html [accessed 29 October 2023].
[47] Probability transformation. https://www.homerenergy.com/products/pro/docs/3.9/probability_transformation.html [accessed 29 October 2023].
[48] R. Dufo-Lopez, J.L. Bernal-Agustin, Design and control strategies of PV-diesel systems using genetic algorithms, Sol. Energy 79 (2005) 33–46, https://doi.org/10.1016/j.solener.2004.10.004.
[49] J.M. Lujano-Rojas, R. Dufo-López, J.S. Artal-Sevil, E. García-Paricio, Searching for promisingly trained artificial neural networks, Forecasting 5 (3) (2023) 550–575, https://doi.org/10.3390/forecast5030031.
[50] S.J. Finch, N.R. Mendell, H.C.J. Thode, Probabilistic measures of adequacy of a numerical search for a global maximum, J. Am. Stat. Assoc. 84 (408) (1989) 1020–1023. https://www.jstor.org/stable/2290078.